Applied Thermal Engineering 290 (2026) 129905

Contents lists available at ScienceDirect

Applied Thermal Engineering

journal homepage: www.elsevier.com/locate/apthermeng

Research Paper

Systematic design and evaluation of a shell-based latent heat thermal energy storage system with a petal shape tube☆

Mohamed Bouzidi [a], Mohammad Hossein Heidarshenas [b], Mohammed Hasan Ali [c], T. Anwor [d], Mansour Mohamed [a], Hammadi Khmissi [e,*], Zehba Raizah [f], Bhupendra Singh Chauhan [g], Mehdi Ghalambaz [h,i,**]

[a] Department of Physics, College of Science, University of Ha'il, Ha'il, P.O. Box 2440, Saudi Arabia
[b] Department of Mechanical and Nuclear Engineering, Kansas State University, Manhattan, KS, USA
[c] College of Technical Engineering, Imam Ja'afar Al-Sadiq University, Al-Muthanna 66002, Iraq
[d] Faculty, of Science, King Mongkut's University, Bangkok, Thailand
[e] Department of Physics, College of Science, Northern Border University, Arar 73213, Saudi Arabia
[f] Department of Mathematics, Faculty of Science, King Khalid University, Abha, Saudi Arabia
[g] Department of Mechanical Engineering, GLA University, Mathura, UP, India
[h] Department of Mathematical Sciences, Saveetha School of Engineering, SIMATS, Chennai, India
[i] Refrigeration and Air Conditioning Technical Engineering Department, College of Technical Engineering, The Islamic University, Najaf, Iraq

ARTICLE INFO

Keywords:
Latent heat thermal energy storage (LHTES)
Phase change material (PCM)
Petal-shaped geometry
Natural convection in PCM
Melting enhancement

ABSTRACT

This study examines a latent heat thermal energy storage (LHTES) unit employing paraffin as the phase change medium and a petal-shaped copper tube heat exchanger represented as a solid non-porous structure. The investigation establishes a geometry-based parametric framework for shell-and-tube LHTES systems by systematically varying petal number and amplitude under constant heat-transfer-fluid (HTF) area, assessing petal-removal to capture the capacity–power trade-off, and analyzing gravity-aligned eccentricity to reveal its coupling with buoyancy effects. Phase change and convection phenomena are simulated using the enthalpy–porosity method with adaptive backward-differentiation time stepping and mesh adaptation. Model predictions show close agreement with validated benchmarks. Results demonstrate that increasing the number of petals from 3 to 8 shortens the melting period from 4081 s to 3286 s (19.5%), while the optimum configuration achieves a 43.6% improvement relative to the circular reference. Raising petal amplitude from 0.10 to 0.25 further reduces melting time by 34.2%, whereas excessive pruning or large eccentricity degrade performance. Moderate petalization and slight radial offset enhance natural convection, accelerating early-stage melting and reducing t_{90}. These findings provide practical, geometry-driven guidance for efficient and manufacturable LHTES design without reliance on porous media or additives.

1. Introduction

To meet the increasing need for reliable and sustainable energy solutions, Latent heat thermal energy storage (LHTES) offers a highly effective method for storing and managing thermal energy. LHTES technology leverages the unique ability of phase change materials (PCMs) to store and release significant thermal energy at a stable temperature during phase transitions [1]. Although LHTES systems offer benefits like compact energy storage and operational simplicity, their widespread adoption remains limited owing to the inherently low thermal conductivity PCMs. [2,3]. Thus, effective enhancement of heat transfer is key to unlocking the practical functionality and economic feasibility of such systems.

Recent studies concur that overcoming low PCM conductivity remains the principal barrier to practical LHTES and motivate geometry-, material- and system-level strategies to increase charging/discharging power while preserving high latent capacity. This includes metal foams [4] finned structures [5], nano-enhanced PCMs [6], and inner-tube/shell geometries specifically tailored to intensify natural-convection

☆ This article is part of a Special issue entitled: 'Cold Storage & Cooling Systems' published in Applied Thermal Engineering.

* Corresponding author.
** Corresponding author at: Department of Mathematical Sciences, Saveetha School of Engineering, SIMATS, Chennai, India.
E-mail addresses: hammadi.ali@nbu.edu.sa (H. Khmissi), ghalambaz.mehdi@gmail.com (M. Ghalambaz).

https://doi.org/10.1016/j.applthermaleng.2026.129905
Received 13 July 2025; Received in revised form 27 October 2025; Accepted 21 January 2026
Available online 24 January 2026
1359-4311/

Nomenclature

Geometry and design
(n_p) Number of petals, –
(r_p) Petal base radius, m
(a) Petal amplitude (length), m
$(a_p = a/r_p)$ Petal amplitude ratio (dimensionless), –
$(e_p = p_c/r_p)$ Radial position of the petal structure (dimensionless)
(d_c) Shell inner diameter, m
$(A_c = \pi d_c^2/4)$ Shell cross-sectional area, m^2
(A_p) Petal cross-sectional area, m^2
$(S \in [0,2\pi])$ Parametric angle rad
$(x(S), y(S))$ Parametric coordinates of petal contour, m
p_c Radial position of the petal structure, m

Fields and properties
$\mathbf{u}$ Velocity vector, m s^{-1}
p Pressure, Pa
θ Temperature, K
θ_f Fusion (melting) temperature, K
$\delta\theta_f$ Phase-change temperature interval, K
θ_w Wall/HTF-side temperature, K
θ_0 Initial PCM temperature, K
ρ Density, kg m^{-3}
μ Dynamic viscosity, Pa s
k Thermal conductivity, W m^{-1} K^{-1}
c_p Specific heat, J/kg K^{-1}
β Thermal expansion coefficient, K^{-1}
$l(\theta)$ Liquid fraction, –
L (h_f) Latent heat of fusion, J/kg

Operators and model constants
I Identity tensor, –
$\boldsymbol{g}$ Gravitational acceleration, m s^{-2}
$F_{(\theta)}$ Mushy-zone momentum sink term, kg m^{-3} s^{-1}
A_{mush} Mushy-zone damping coefficient, Pa s m^{-2}
Γ Stabilization parameter, –
A_μ Solid-phase viscosity scaling factor, Pa.s
$\boldsymbol{n}$ Outward unit normal vector, –

Global measures and numerics
MVF Melted volume fraction, –
$Q_{sensible}$ Sensible heat, J/m
Q_{latent} Latent heat, J/m
$Q_{store} = Q_{sensible} + Q_{latent}$ Total stored heat, J/m
Nm Mesh density, –

Acronyms
LHTES Latent heat thermal energy storage, –
PCM Phase change material, –
Hp Heat pipe, –
NePCM Nano-enhanced phase change material, –
HTF Heat transfer fluid, –
BDF Backward differentiation formula, –
FEM Finite element method, –
PDE Partial differential equation, –

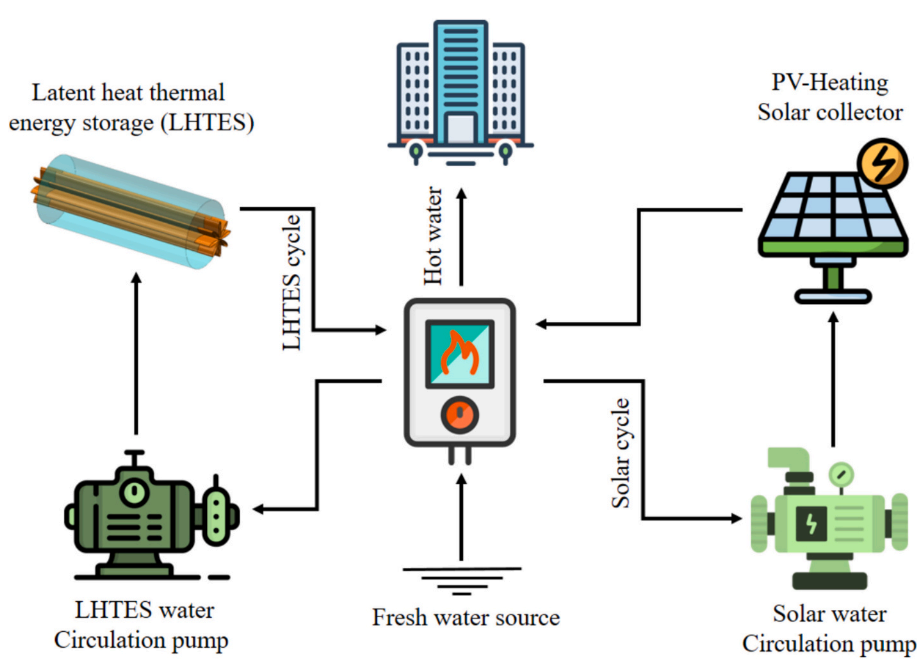

Fig. 1. System's components of LHTES unit.

pathways in horizontal shell-and-tube units [7].

Addressing this challenge, one fundamental issue in LHTES is the occurrence of dead zones, regions characterized by slow melting or solidification of PCM. Dead zones develop due to non-uniform heat distribution, significantly affecting charging and discharging rates. The use of metallic fins, a common strategy for enhancing heat transfer, effectively addresses these issues by guiding heat flow directly toward these problematic regions. Detailed studies highlight that optimizing fin parameters, such as their length, orientation, and spacing, can drastically improve heat transfer efficiency and reduce the impact of dead zones [8]. Comparative assessments since 2022 show that fin topology (solid vs. perforated), orientation, and hybridization with metal foams increase interfacial area and shorten melting time, with the most effective designs balancing added surface with acceptable pressure drop and

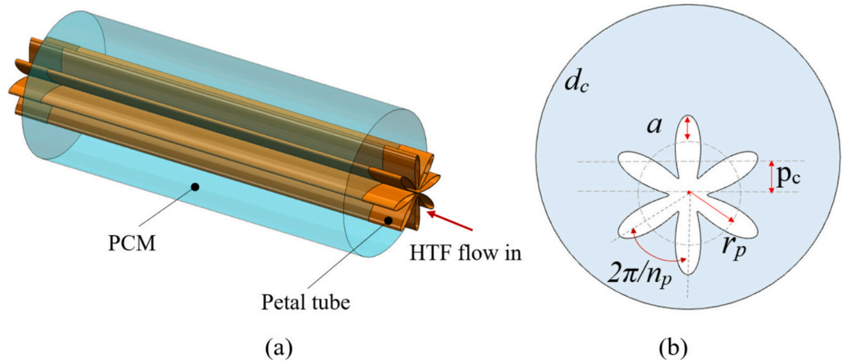

Fig. 2. Petal shape HTF in a LHTES unit (a) 3D view of the LHTES and (b) cross-section of the model and geometrical details of the system.

Table 1
Material properties for paraffin wax and copper foam.

Materials	C_p (J/kg.K)	ρ (kg/m^3)	k (W/m.K)	μ (Pa.s)	T_{fu} (K)	Fusion Enthalpy (J/kg)	β (1 K^{-1})
Paraffin (solid/liquid) [35–38]	2700/2900	916/790	0.21/0.12	0.0036	324.65	176,000	0.0009
Copper foam [39]	386	8900	380	–	–	–	–

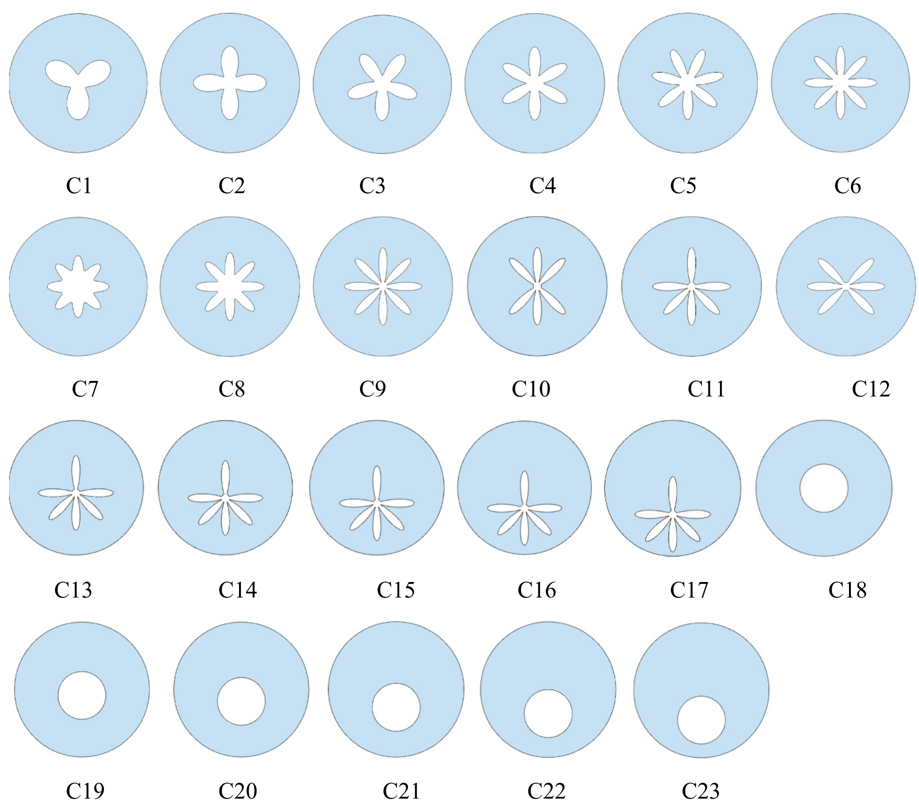

Fig. 3. A schematic-geometrical view of the investigated cases.

manufacturability [9]. Zhang et al. [5] examined the thermal behavior of a latent heat thermal energy storage tube equipped with longitudinal fins. They reported oscillatory behavior in the PCM close to the HTF tube, which was attributed to the onset and evolution of natural convection within the melted PCM region. Hamid and Mehrdoost [10] numerically studied a shell-and-multiple-tube LHTES using paraffin RT35, evaluating sinusoidal wavy fins, tube number, and tube shape at constant material volume. Double-pitch wavy fins cut melting time 9.5% versus straight fins. Increasing HTF tubes from one to four reduced melting time 38.3%.

Heat pipes (HPs) also offer significant promise in enhancing LHTES performance, primarily by improving the thermal conductivity between PCM and external heat sources or sinks. Various coupling strategies, such as embedding HPs entirely within PCM or integrating them selectively at evaporation or condensation sections, can greatly enhance heat transfer efficiency [2]. However, research indicates that a more holistic design approach, considering the interplay between HP and PCM thermal characteristics, is essential for future advancements [2]. This would

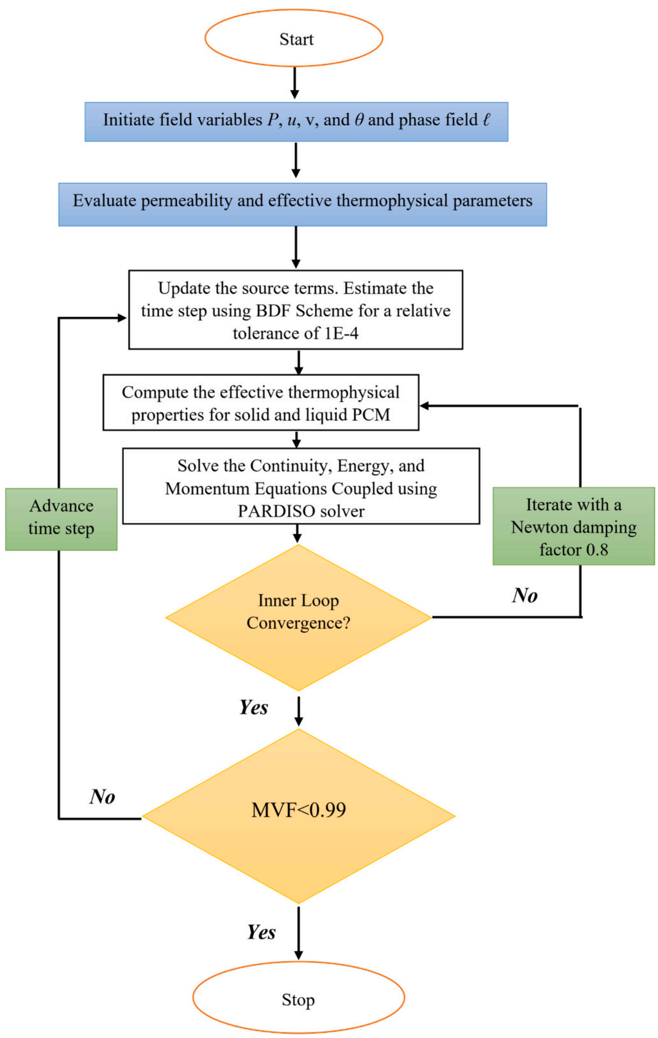

Fig. 4. The FEM code implication and BDF time-step for error management.

Table 2
The mesh parameter values and their corresponding mesh quality characteristics.

Nm	Edge elements	Triangles	Quads	Total Elements
1.0	999	14,101	1888	15,989
1.25	1175	19,811	2352	22,163
1.5	1360	27,720	2816	30,536
1.75	1527	35,301	3280	38,581
2.0	1682	43,208	3760	46,968
2.25	1832	51,826	4224	56,050
2.5	1971	61,343	4688	66,031

Selected Mesh Nm = 2.0.

require detailed multi-scale simulations linking microscopic phase-change behaviors to macroscopic heat transfer performance. While HP-PCM coupling is effective, recent surveys emphasize that passive geometric control of natural convection in shell-and-tube LHTES can deliver comparable acceleration with lower system complexity, particularly when the inner-tube shape and placement are optimized to trigger plume formation and enlarge molten channels [11].

Innovative techniques such as nano-enhanced PCMs (NePCMs) represent another frontier in the development of high-performance LHTES systems. Incorporating nanoparticles significantly increases thermal conductivity and accelerates charging and discharging rates by over 40% [3]. Updated syntheses report conductivity gains typically in

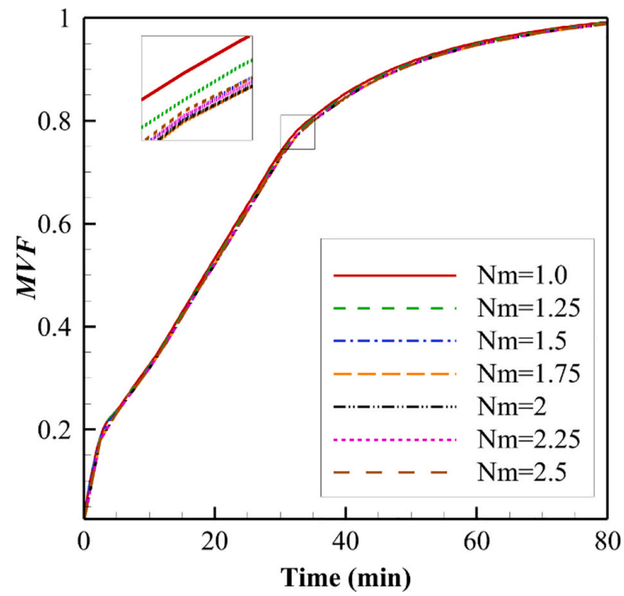

Fig. 5. Mesh independence analysis for six different values of mesh parameter *Nm = 1.00, 1.25, 1.50, 1.75, 2.00, 2.25 and 2.50.*

the 10–50% range for dilute loadings, with larger gains when nanoparticles are integrated within porous/foam matrices; however, stability, cost, and viscosity penalties motivate exploring geometry-first enhancements in parallel [12].

Moreover, enhancing interfaces between PCM and heat transfer fluids (HTFs) is equally vital. Studies comparing flat, extended, and direct-contact interfaces clearly illustrate that diversified and extensible interfaces significantly boost heat transfer performance [13]. Advanced interface structures facilitate improved thermal accessibility, directly addressing challenges posed by PCM's limited thermal conductivity. Practical applications, such as thermal management in battery systems, further exemplify the importance of optimized LHTES systems. Innovative designs, including mutually embedded fins and integrated PCM layers in battery packs, effectively stabilize operational temperatures, significantly enhancing battery life and performance [14,15].

The inner tube and body shapes significantly influence heat transfer enhancement within enclosures, particularly under conditions of natural convection, a mode of heat transfer driven by buoyancy effects due to temperature gradients. The presence and geometry of internal geometries, such as square, circular, elliptical, and petal-shaped objects, directly both flow dynamics and thermal fields within enclosures, which has been widely validated through both numerical and experimental studies [16,17]. Internal bodies can modify flow characteristics by altering fluid patterns, which in turn affects heat transfer rates significantly. For instance, enclosures with circular or elliptical bodies generally exhibit more streamlined flow paths, while rectangular or complex geometries like petal-shaped structures create stronger recirculation zones, enhancing convective heat transfer [18–20]. Vigorous fluid motion is essential for maximizing heat-transfer efficiency, with greater circulation intensities generally yielding improved heat transfer coefficients and higher Nusselt numbers [18]. Recent work clarifies that shell shape and inner-tube layout can raise stored energy and shorten phase-change duration even at fixed PCM volume, underscoring geometry as a first-order design variable in horizontal LHTES [21].

Furthermore, recent developments highlight the benefits of using specialized surface features on internal tubes, such as dimples and protrusions arranged in petal-like patterns. These features significantly improve heat transfer efficiency by promoting turbulence and destabilizing the thermal boundary layer, which enhances both condensation and evaporation processes [22]. For latent heat storage, non-circular and multi-lobe inner tubes (e.g., polygonal, I-beam, and petal-like

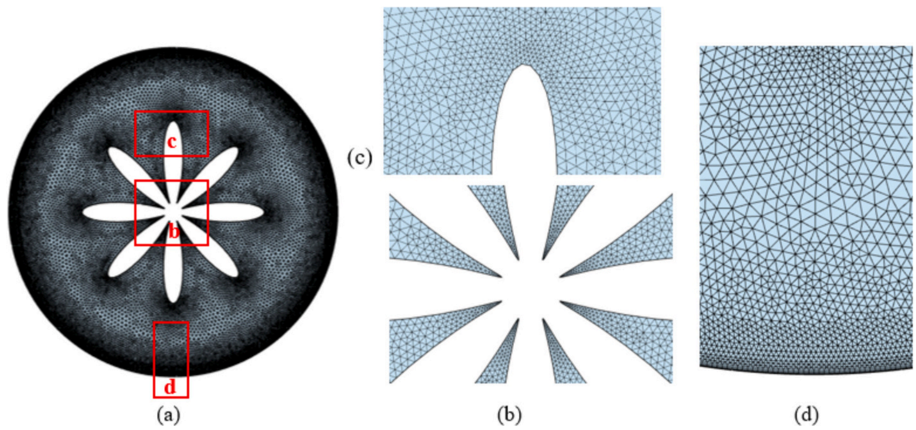

Fig. 6. Mesh density and distribution for $Nm = 2$ at (a) the whole domain (b and c) petal corners (d) shell wall.

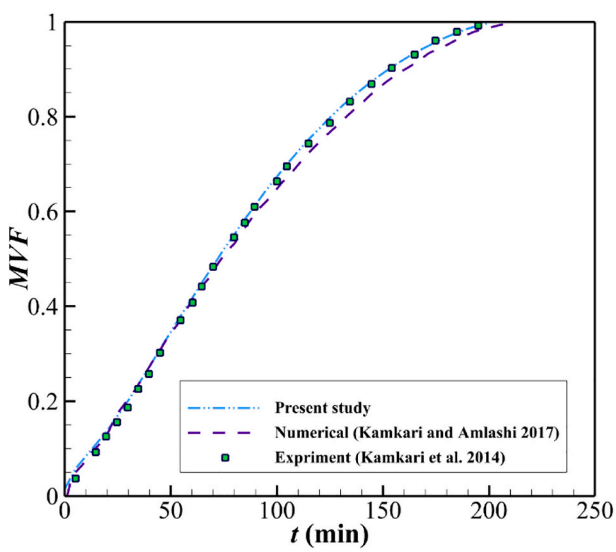

Fig. 7. Comparison of the melted volume fraction between the present simulation and the experimental data reported by [44,45].

geometries) strengthen plume formation near sharp tips and edges and widen the melted channels. As a result, the system reaches MVF $\approx$ 0.9 more quickly than comparable circular tubes. Although studies on fully petal-shaped tubes in LHTES are still emerging, recent numerical work consistently shows faster initial melting and higher overall melt fractions compared with equal-area circular tubes [23,24]. In the study by Shafi et al. [24], a bundle of petal tubes was embedded in a composite metal foam–PCM system, so natural convection was affected by tube–tube interactions and by the presence of the metal foam. In contrast, in the present study the petal tube is embedded in a single shell without metal foam.

The shape of inner tubes and the addition of fins critically impact the performance of PCMs within thermal storage enclosures. Given the inherently low thermal conductivity of PCMs, optimizing geometry and enhancing internal structures like fins are pivotal for efficient heat transfer and effective phase transitions [25]. Rectangular and annular container geometries have shown significant advantages, particularly rectangular shell-tube configurations which effectively utilize buoyancy-induced natural convection for enhanced heat distribution, resulting in increased melting rates and shorter phase-change times [25,26]. Annular tube eccentricity, a simple yet highly effective design approach, markedly influences the heat absorption and release characteristics of PCM thermal storage units. Studies demonstrate that optimized eccentricity significantly reduces PCM charging time by facilitating more uniform heat distribution, although it may slow down the discharge process, making it particularly beneficial for passive thermal management in energy-efficient buildings [27].

Moreover, elliptical inner tubes with optimized aspect ratios and inclination angles significantly improve the phase-change performance. Adjusting these parameters enhances the convective currents within the PCM, thus minimizing melting times and optimizing energy storage efficiency [28]. Wavy inner tubes and elliptically shaped double tubes further accelerate PCM melting and solidification processes by enhancing surface area and inducing turbulence, especially when combined with nanoparticles, greatly improving heat distribution within the enclosure [29]. Fins within PCM storage systems substantially enhance heat transfer by providing additional conductive paths and promoting natural convection currents. Experimental results confirm that finned-tube configurations significantly outperform non-finned designs, achieving higher thermal energy storage capacities and improved charging and discharging rates [30].

The shape of the HTF tubes within LHTES enclosures significantly impacts phase-change efficiency, playing an important role in enhancing thermal efficiency. Changing the geometry of HTF tubes, from traditional circular designs to more innovative shapes such as petal, polygonal, or elliptical, enhances heat transfer due to improved fluid dynamics and thermal interaction with PCMs [31,32]. Research demonstrates substantial improvements in melting and solidification rates when employing non-circular tube geometries. For instance, I-beam and polygonal tubes considerably reduce charging and discharging times compared to standard circular tubes, with performance gains attributed to increased surface areas and optimized thermal convection pathways [23,32]. Recent analyses explicitly link multi-lobe edges and sharp tips to earlier boundary-layer destabilization and plume coalescence, explaining faster increases in mean volumetric melt fraction compared with smooth circular counterparts [23]. For petal-like geometries, newly reported foam-assisted and metal-foam-free configurations show accelerated early-time melting and shorter t_{90} relative to circular baselines at equal cross-sectional area [24].

The literature review shows that the HTF shape can significantly influence thermal transport and fluid circulation during phase change inside an enclosure. A petal-shaped HTF tube can provide mechanical strength and an extended heat transfer surface between the internal heat transfer fluid and the surrounding PCM in an LHTES unit. However, there is a gap in understanding how the configuration of petals, changes in eccentricity, and removal of unnecessary petal sections can influence the heat transfer rate without reducing the energy storage capacity. The current work explores, for the first time, the effects of petal configuration and distribution on melting heat transfer.

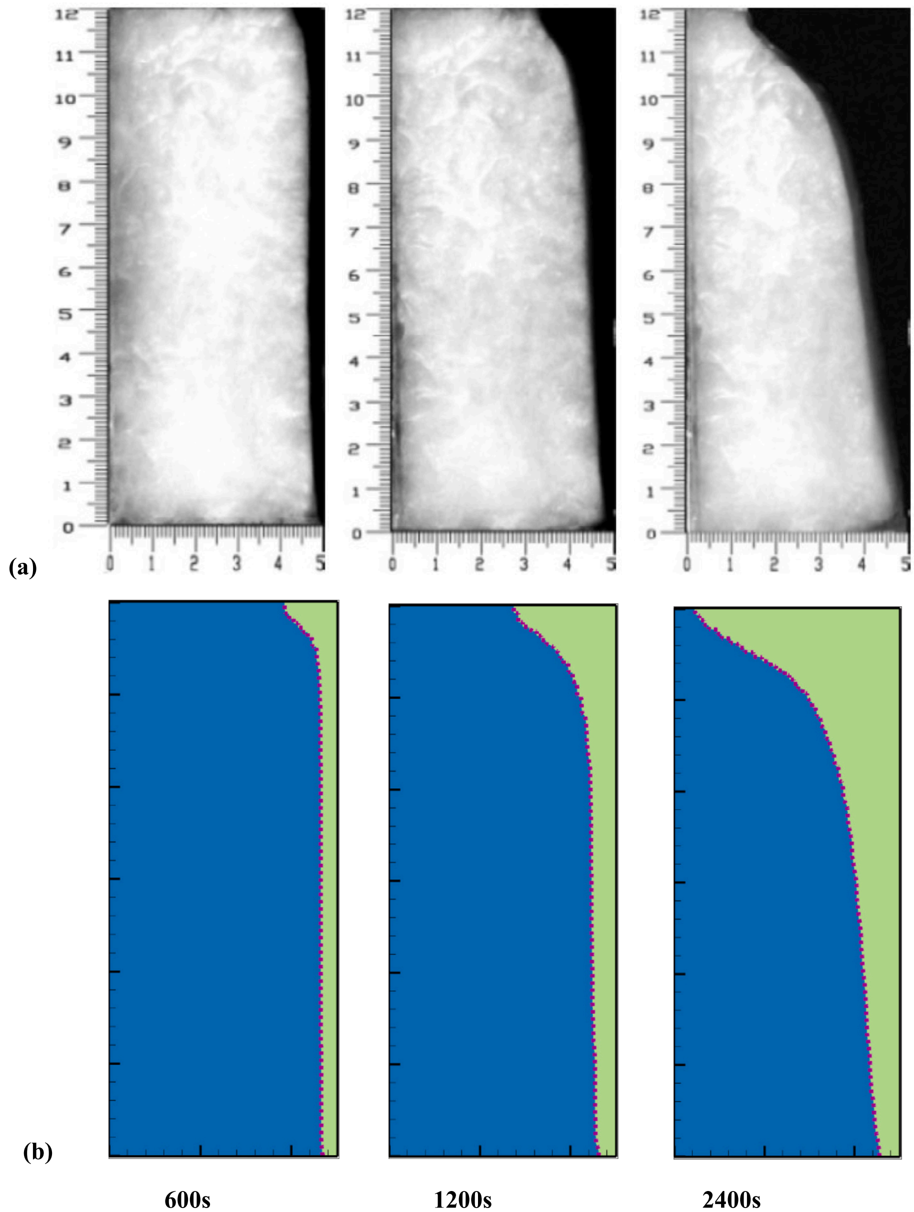

Fig. 8. Comparison of fusion lines during the melting process: (a) experimental results reported by [44], and (b) the Results from the current numerical simulation.

2. Model description and mathematical modeling

Concentrated solar heating systems, especially those integrated with LHTES, play an essential role in enhancing technology in solar energy. Given the inherently intermittent nature of solar energy due to the meteorological variability LHTES systems are valuable for maintaining consistent energy supply. They can store large quantities of thermal energy in a compact space at fusion temperatures, smoothing out fluctuations during variable solar input [33,34].

As shown in Fig. 1, a typical system consists of a solar collector, circulation pumps, an LHTES module, and a hot water storage tank. The collector transfers heat to water, which is subsequently retained in the tank in the form of latent thermal energy to provide hot water to the building as needed. A regulated circulation loop connects the thermal storage tank with the LHTES module. When energy demand is low or generation is high, the pump activates to transfer excess heat into the LHTES. In the opposite way, during low solar output, the tank extracts the reserved thermal energy from the latent heat storage system.

Fig. 2 illustrates the configuration of an LHTES unit employing a shell–petal tube design. The device's structure consists of a shell and a HTF petal tube. Fig. 2a shows a 3D view of the LHTES where the HTF flows into the petal-shaped tube at a high temperature, denoted as T_{h}, and exists from the other side. The shell side is filled by paraffin, PCM, at a supper cold temperature T_0. Fig. 2b depicts a 2D view of the model and geometrical details of the system. The petal shape is controlled by number of the petals and the petal amplitude. The petal-shaped geometry is represented by a polygon based on given x and y coordinates [31].

$$\begin{cases} x = \left(r_b + a\sin\left(n_p \times S\right)\right)\cos(S) \\ y = \left(r_b + a\sin\left(n_p \times S\right)\right)\sin(S) \end{cases} \tag{1}$$

where $S = \{0, 0.03, 0.06, \ldots, 2\pi\}$. While the number and amplitude of petals are changed, the area of the petal remains unchanged. Therefore, in all cases, the quantity of PCM remains identical. Here, n_p is the petal number, and a is the amplitude of the petal. The petal shape can be moved or rotated using p_c defined as the offset between the circle center and the petal center, d_c corresponds to the shell tube diameter, and r_p is the petal base radius. Some of the petals can also be removed which in this case leads to an increased PCM mass occupying the domain.

Table 3
Designed cases and parameter details with corresponding value of MVF for 90% charge.

Case	Goal	(n_p)	(a_p)	e_p	Melting time (s) for MVF = 0.9
C1		3	0.20	0	4081
C2		4	0.20	0	4010
C3		5	0.20	0	3681
C4	(n_p)	6	0.20	0	3517
C5		7	0.20	0	3429
C6		8	0.20	0	3286
C7		8	0.10	0	4412
C8	(a_p)	8	0.15	0	3775
C9		8	0.25	0	2904
C10		8	0.25	0	3303
C11	Petal prune	8	0.25	0	2980
C12		8	0.25	0	3541
C13		8	0.25	1/4	2695
C14		8	0.25	1/2	2675
C15	Petal radial offset	8	0.25	3/4	2856
C16		8	0.25	1	3119
C17		8	0.25	5/4	3421
C18		0	0	0	5822
C19		0	0	1/4	4916
C20		0	0	1/2	4343
C21	Reference	0	0	3/4	4247
C22		0	0	1	4352
C23		0	0	5/4	4760

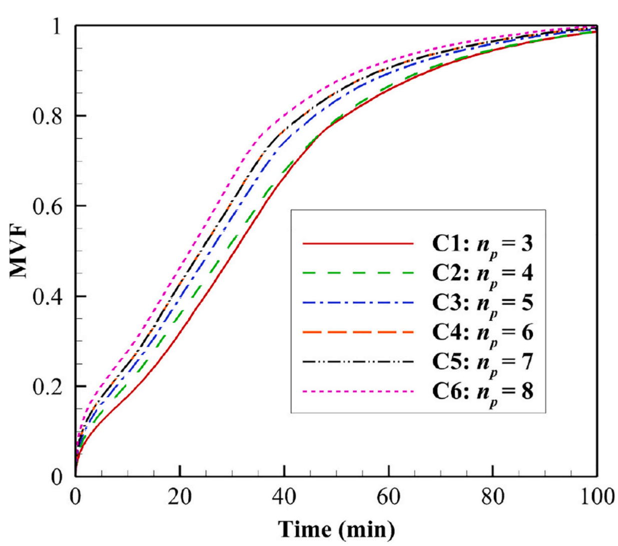

Fig. 9. Impact of petal number on the MVF during the charging process.

When petals are present, the petal-shaped HTF tube protrudes into the shell region and occupies part of the available cross-section that would otherwise be filled by PCM. In the subset of geometries where only the number of petals and their amplitude are varied, the internal HTF cross-section is held constant; consequently, the PCM quantity remains unchanged across those cases. By contrast, in the "petal-removal" configurations the shell diameter is kept fixed while one or more petals are omitted. Removing petals decreases the space taken by the HTF tube and frees additional shell volume for the PCM. Over the same device length, this directly increases the mass of PCM contained in the shell.

This geometric change also carries a performance trade-off. Petals act like fins that enlarge the HTF–PCM contact perimeter and enhance heat transfer into the low-conductivity PCM. Omitting petals reduces that interfacial area and the associated fin effect. As a result, petal removal increases the nominal energy capacity (because more PCM is present and the latent heat listed for paraffin in Table 1 scales with PCM mass) but can lengthen melting and solidification times compared with multi-petal cases. In short, the petal-removal subset favors storage capacity, whereas the multi-petal subset favors heat-transfer power. To make this distinction transparent, Fig. 3 groups the geometries accordingly: cases with petals (e.g., C1–C17) maintain a constant HTF cross-section and therefore a constant PCM quantity, while the annular or reduced-petal cases (C18–C23) intentionally shrink the HTF cross-section, increasing the PCM volume occupying the shell.

Table 1 provides the physical and thermal characteristics of both paraffin wax and copper foam. The following geometrical details were used: $d_c = 40$ mm. The shell surface area is computed as $A_c = \pi d_c^2/4$ and the area of petal (A_p) is fixed as $A_p = A_c/8$. Then, the petal basis radius (r_p) is computed as $r_p = \sqrt{\frac{A_p}{\pi} - \frac{a_p^2}{2}}$, and amplitude ratio ($a_p$) is introduced as $a_p = a/r_p$. The petal eccentricity ratio is also evaluated as $e_p = p_c/r_p$.

As shown in Fig. 3, various cases have been considered to investigate the impact of petal shape on the phase change dynamics. All 23 cases comprehensively cover the study of petal number and amplitude. By independently increasing the petal numbers and adjusting their locations, the effect of each parameter has been investigated and presented in the results section.

The 23 geometries are organized in two groups. C1–C17 (multi-petal, constant HTF area), the petal number n_p and petal amplitude are varied while the HTF cross-sectional area is held constant; consequently, the PCM quantity is unchanged across C1–C17. C18–C23 (petal-removal/annular), one or more petals are omitted, reducing the HTF cross-section and increasing the PCM volume within the shell; these cases form an annular family with progressively larger PCM occupancy.

2.1. Governing equations

To capture the interface dynamics between solid and liquid phases, the enthalpy–porosity method was applied in this work. In this approach, the entire computational domain was modeled as a porous medium with spatially varying porosity. The porosity value varies between 0 (solid) and 1 (liquid), corresponding to the phase state of the PCM at each location. Areas that are completely solid are given a value of 0, while regions with fully liquid PCM are assigned a porosity of 1. The mushy zone, which is defined by intermediate porosity values ranging from zero to one, where the PCM is partially melted. By employing this method, the dynamic movement of the phase interface can be effectively captured. [40–42].

I) Mass conservation

$$\nabla \cdot \boldsymbol{u} = 0 \tag{2}$$

II) Momentum equations

$$\rho_{PCM,l}\frac{\partial \boldsymbol{u}}{\partial t} + \rho_{PCM,l}(\boldsymbol{u}\cdot\nabla)\boldsymbol{u} = \nabla\cdot\left[-pI + \mu_{PCM,l}\left(\nabla\boldsymbol{u} + (\nabla\boldsymbol{u})^T\right)\right] + (\rho\beta)_{PCM,l}\boldsymbol{g}\left(\theta - \theta_f\right) + F(\theta)\boldsymbol{u} \tag{3}$$

where

$$F(\theta) = A_{mush}\frac{1 - 2\ell(\theta) + \ell^2(\theta)}{\Gamma + \ell^3(\theta)}; A_{mush} = 1\times10^6 Pa.s\Big/m^2 \ and\ \Gamma = 10^{-3} \tag{4}$$

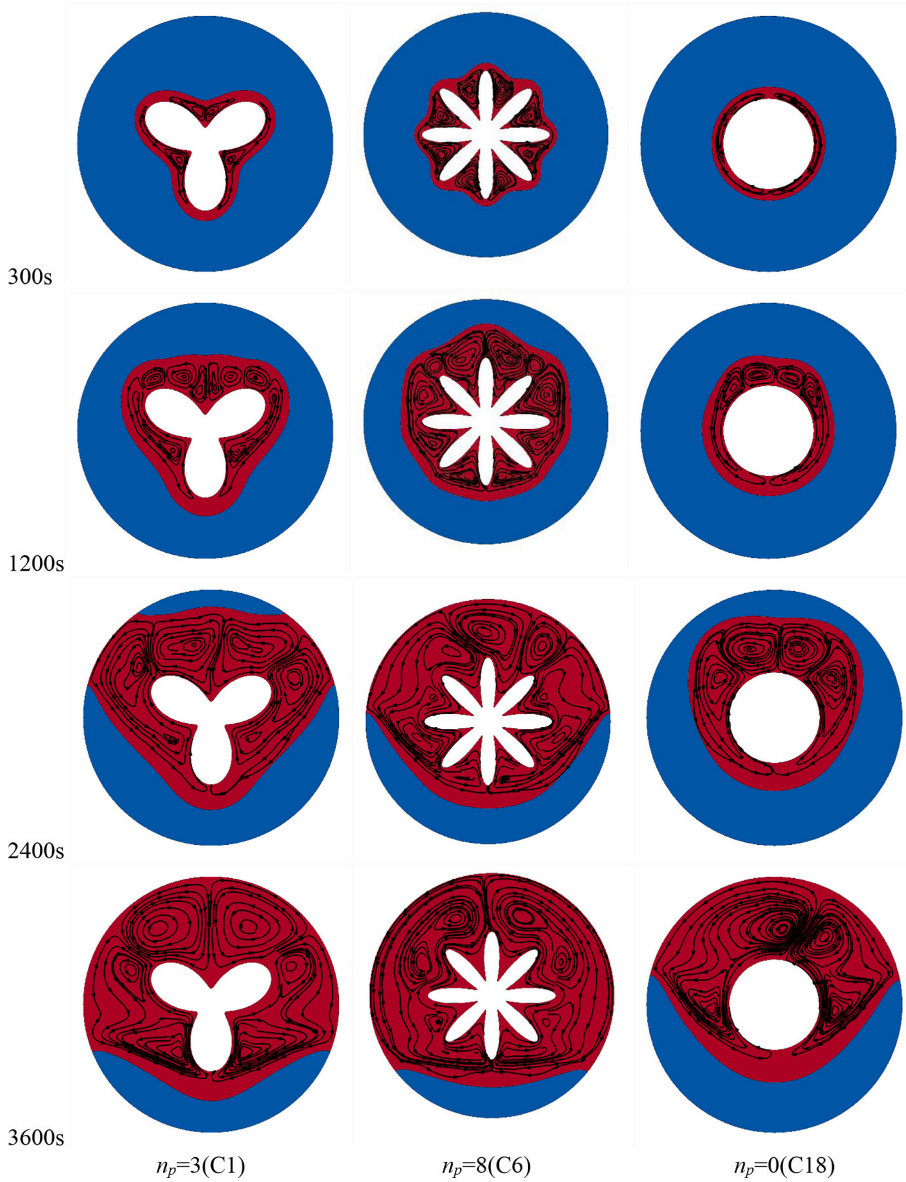

Fig. 10. (a). Impact of the petal number on melting process for $n_p = 3$ (C1), $n_p = 8$ (C6), $n_p = 0$ (C18) at times: 300 s, 1200s, 2400 s, 3600 s. (b). Impact of petal number on the thermal distribution for $n_p = 3$ (C1), $n_p = 8$ (C6), $n_p = 0$ (C18) at times: 300 s, 1200s, 2400 s, 3600 s.

and

$$\boldsymbol{g} = \begin{cases} 0 & x \\ g & y \end{cases} \tag{5}$$

In this context, μ is the dynamic viscosity, ρ is density, and ℓ is the liquid-phase fraction of the PCM. Across the PCM domain, and based on the local temperature, ℓ indicates the locally defined liquid ratio, bounded between 0 and 1. When $\ell = 1$, the substance is fully melted; $\ell = 0$ represents the fully solid state, while $0 < \ell < 1$ characterizes the mushy zone with both phases present. During the melting or solidification process, this time-dependent field varies across space and changes according to the Eq. (6). The time is t, θ represents the temperature field, and u denotes the velocity vector. A piecewise polynomial-based approximation technique is applied to determine the PCM properties within the mushy region.

$$\ell(\theta) = \begin{cases} 0 & \theta \le \theta_f - \dfrac{\delta\theta_f}{2} \\ \dfrac{\theta - \theta_f}{\delta\theta_f} + \dfrac{1}{2} & \theta_f - \dfrac{\delta\theta_f}{2} < \theta < \theta_f + \dfrac{\delta\theta_f}{2} \\ 1 & \theta \ge \theta_f + \dfrac{\delta\theta_f}{2} \end{cases} \tag{6}$$

where, the phase change range is $\delta\theta_f = 5^\circ C$.

III) Governing Equation for Energy Conservation in the PCM

$$(\rho c_p)_{PCM}\frac{\partial\theta}{\partial t} + (\rho c_p)_{PCM,l}\boldsymbol{u}.\nabla\theta = \nabla.(k_{PCM}\nabla\theta) - \rho_{PCM}h_{PCM}\frac{\partial\ell(\theta)}{\partial t} \tag{7}$$

where k denotes the thermal conductivity, h refers to the latent heat associated with the melting process and c_p is the specific heat capacity. The subscription of l indicates the liquid PCM while s represents the solid PCM. The thermal and physical characteristics of the PCM within the

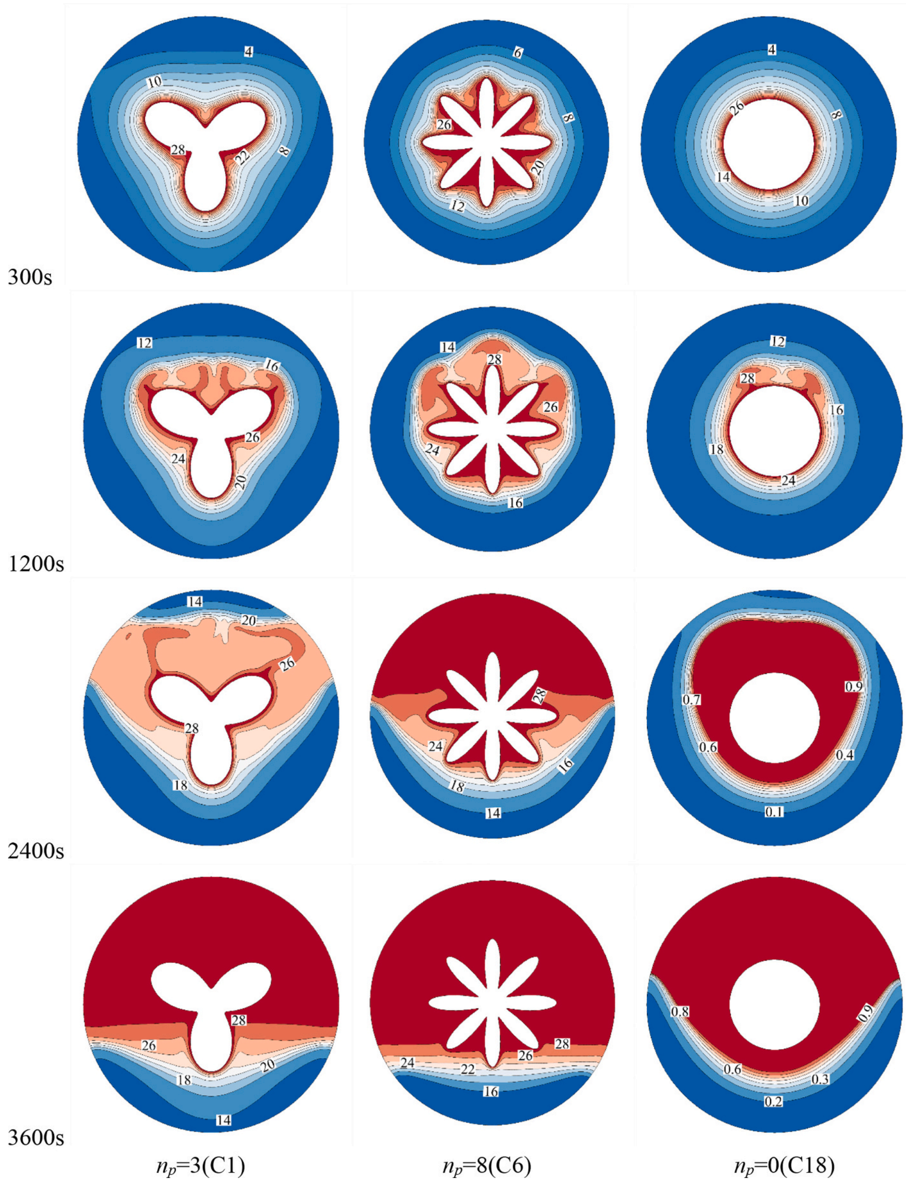

Fig. 10. (*continued*).

mushy region such as specific heat, density, and thermal conductivity, are determined by linear interpolation based on the local liquid fraction $\ell(\theta)$, as defined in Eqs. (8)–(10).

$$(\rho c_p)_{PCM} = \ell(\theta)\left[(\rho c_p)_{PCM,l} - (\rho c_p)_{PCM,s}\right] + (\rho c_p)_{PCM,s} \tag{8}$$

$$\rho_{PCM}(\theta) = \ell(\theta)\left(\rho_{PCM,l} - \rho_{PCM,s}\right) + \rho_{PCM,s} \tag{9}$$

$$(k)_{PCM}(\theta) = \ell(\theta)\left[(k)_{PCM,l} - (k)_{PCM,s}\right] + (k)_{PCM,s} \tag{10}$$

To avoid numerical instabilities and unphysical flow in solid PCM regions, a liquid-fraction-dependent viscosity model was applied. The viscosity, μ is given by $\mu = A_\mu\,(1\text{-}\ell) + \mu_{PCM,\,l}$ where A_μ set to 1×10^4 Pa.s serves as a damping factor that increases the viscosity as the material approaches the solid phase, thereby minimizing spurious velocities.

It should be emphasized that the mushy zone is considered an internal transition region within the domain, controlled by the melt fraction field $\ell(\theta)$, described in Eq. (6). This zone's distribution is affected by both the domain's thermal gradient and the selected phase change interval, $\delta\theta_f$. The method allows for a gradual phase transition, with the mushy region dynamically evolving in shape and thickness based on geometry and active heat transfer processes during simulation. The free convection in the liquid domain was considered using the momentum equation coupled with the Boussinesq approximation buoyancy term. When the PCM reaches the liquid state ($\ell = 1$) this term becomes active, enabling fluid motion driven by thermal expansion and temperature gradients distributed across the domain.

In enthalpy-porosity modeling, the use of a large viscosity value for solid PCM is a widely adopted approach. The approach introduces a momentum sink that suppresses fluid motion in non-melted areas, approximating a no-flow boundary. Preliminary simulations confirmed that the selected value of $A_\mu = 10^4$ Pa supports solver robustness and convergence. Instabilities observed with reduced or zero A_μ values confirm the need for a strong damping coefficient in solid zones.

Specific boundary and initial conditions are applied to the physical domain. Periodic thermal boundary conditions were applied to the outer hexagonal walls. During melting, the petal tube wall was kept at $\theta_w = \theta_f + 15$ °C, and the PCM domain was initialized at $\theta_0 = \theta_f - 15$ °C, ensuring a fully solid starting condition. In contrast, during the solidification phase, the tube wall temperature was set to $\theta_w = \theta_f - 15$ °C, while the

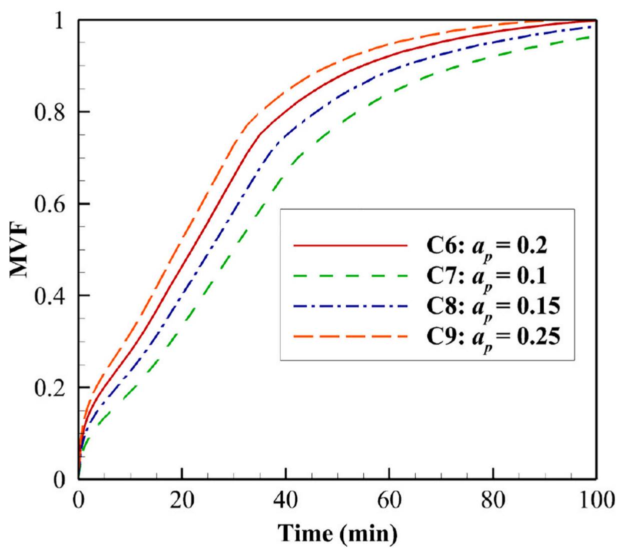

Fig. 11. Impact of petal amplitude on the MVF during the charging process.

initial domain temperature was set to $\theta_0 = \theta_f + 15\ ^\circ\mathrm{C}$ ensuring the PCM was entirely in the liquid phase.

Zero initial conditions were applied for both velocity and pressure fields over the entire computational domain. All physical boundaries were treated as no-slip and impermeable ($u = v = 0$), The bottom-left corner was set to zero gauge pressure to define a reference point for the pressure field. Periodic boundary conditions in finite element approach, were implemented by matching nodes on opposing boundaries, ensuring equal temperatures and heat fluxes across corresponding degrees of freedom.

On the petal surface:

$$\theta = \theta_w, \tag{11a}$$

and the zero heat flux on the shell surfaces was applied as:

$$\frac{\partial \theta}{\partial n} = 0 \tag{11b}$$

with n denotes the unit normal vector to the surface.

The volume fraction of melting indicates the portion of the material that has transformed into the liquid phase. The value is obtained by dividing the molten region volume by the complete domain volume and can be formulated as:

$$MVF = \frac{\oint_A \ell dA}{\oint_A dA} \tag{12}$$

The system's total thermal energy includes both sensible heat, associated with temperature changes, and latent heat, associated with phase transitions. The total thermal energy is calculated based on the following set of equations:

$$Q_{sensible} = \left[\oint_{PCM} \left(\int_{\theta_0}^{\theta} (\rho C_P)_{PCM}(\theta) d\theta \right) dA \right] \tag{13a}$$

$$Q_{latent} = \oint_{PCM} \rho_{PCM} \ell L_{PCM} dA \tag{13b}$$

where dA is the element of domain area.

Q_{store} represents the total energy stored, consisting of sensible and latent heat:

$$Q_{store} = Q_{sensible} + Q_{latent} \tag{13c}$$

$U = |\overrightarrow{u}|$ is the magnitude of the liquid velocity (U) in the domain.

3. Solution approach

3.1. Numerical approach

As a powerful numerical approach, the finite element method (FEM) serves as a robust computational tool for addressing coupled partial differential equations (PDE) governing fundamental physical processes such as mass, momentum, and energy conservation. This method discretizes the domain into finite elements and employs basis functions to approximate the solution within each element. As a result of the discretization process, by discretizing continuous field equations, FEM yields algebraic systems that can be efficiently solved with high accuracy.

A fundamental step in the FEM formulation is the transformation of the governing PDEs into their corresponding weak formulation. This process, known as the Galerkin method, involves multiplying the governing equations by test functions and integrating the resulting expressions over the entire domain. The weak form simplifies the equations by reducing derivative order, usually replacing second-order terms from the strong form with first-order expressions. As a result, the weak form is more compatible with numerical methods and flexible in handling a wider variety of boundary condition types.

The global system was constructed using Gauss quadrature to compute element integrals, resulting in nonlinear residual equations. Continuity, momentum, and energy residuals were iteratively resolved via the Newton-Raphson method coupled with the PARDISO direct solver, convergence stability was improved by introducing a damping factor of 0.8. Fig. 4. Shows a brief flow diagram of the implemented code structure. A convergence tolerance of 10^{-3}, based on the relative residual norm, was imposed. Moving to the next time step occurred only after this criterion was met, ensuring numerical accuracy at each iteration [43].

The governing equations were integrated in time using a variable-order Backward Differentiation Formula (BDF), ranging from first to second order. An adaptive time-stepping scheme was employed according to approximations of the local truncation error. When the convergence was fast and the solution remained stable, the solver adapted by increasing the time step or switching to a higher BDF order, to improve computational performance. Similarly, the solver reduced the time step and lowered the BDF order in areas with sharp gradients or strong nonlinear behavior to ensure numerical stability. This adaptive strategy helped the solver balance accuracy and speed during the simulation.

3.2. Mesh study

Given the mesh-dependent behavior of computational models, grid sensitivity analysis serves as a key step in verifying simulation accuracy and robustness. Mesh that is too coarse or badly designed can cause errors or slow down the solution, while a well-chosen mesh can improve both accuracy and speed of the simulation. Therefore, to confirm the validity and stability of the numerical results for case C9, grid refinement studies are performed. Mesh resolution is controlled by the parameter Nm. As increase in Nm leads to a larger number of elements and thus a finer grid. Table 2 shows the details of utilized meshes. The simulations were conducted for all mesh sizes of Table 2. Fig. 5 illustrates the evolution of the melting volume fraction (MVF) over time for different mesh resolutions (Nm parameter). As seen, an increase of Nm slightly changes the curves. Thus, in this study, mesh case $Nm = 2$ was selected as the optimal resolution to ensure sufficient accuracy for the numerical model.

A triangular unstructured mesh was employed to ensure detailed discretization over the entire computational domain. A magnified view of the mesh at petal corners and shell wall is illustrated in Fig. 6.

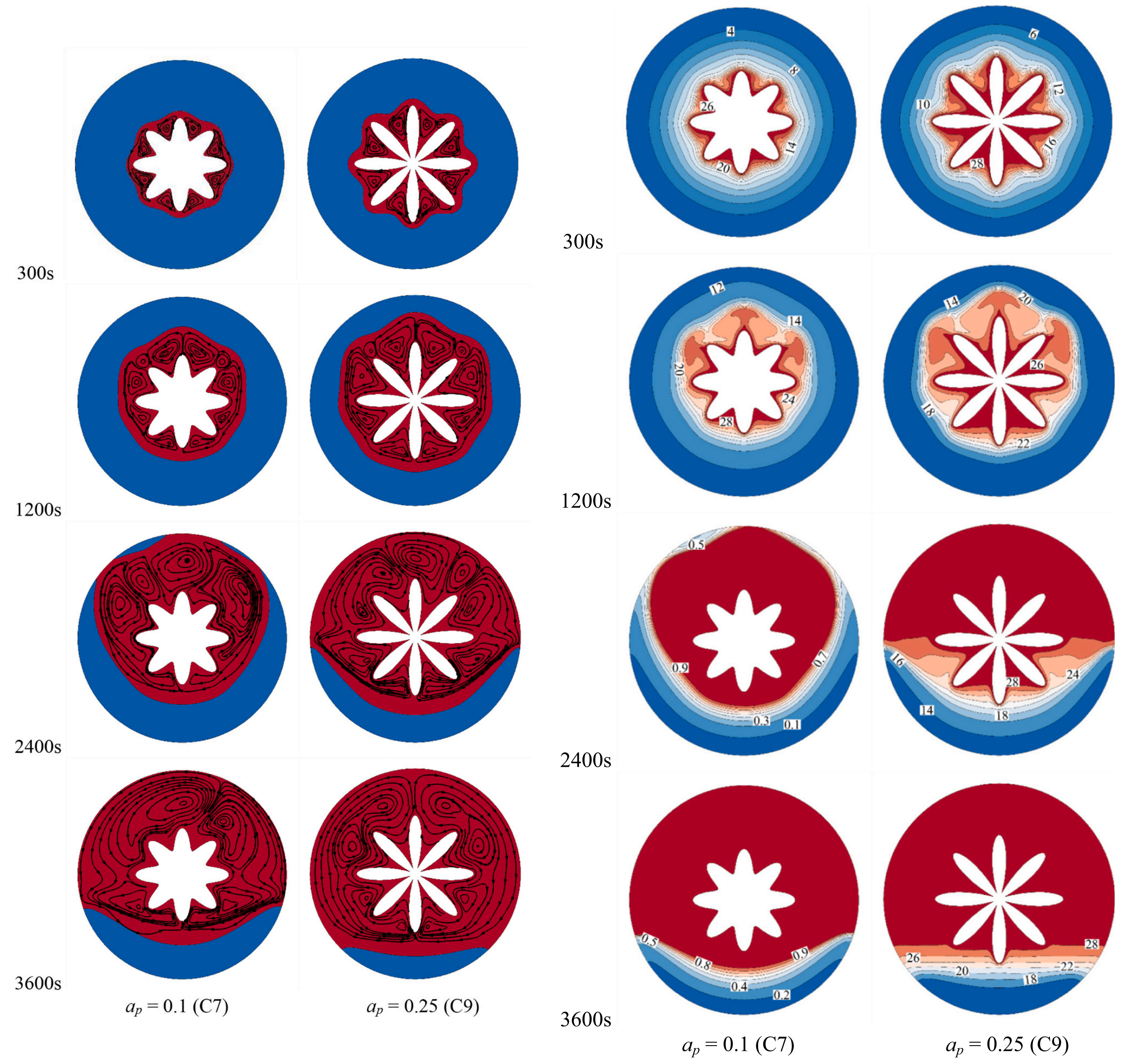

Fig. 12. (a) Impact of the petal amplitude on melting process for $a_p = 0.1$ (C7), $a_p = 0.25$ (C9) at times: 300 s, 1200s, 2400 s, 3600 s. (b) Impact of petal amplitude for thermal distribution for $a_p = 0.1$ (C7), $a_p = 0.25$ (C9) at times: 300 s, 1200s, 2400 s, 3600 s.

3.3. Validation and verification

The model's accuracy and reliability are evaluated by comparing its predictions with validated numerical and experimental data reported in the literature. The phase changing dynamics of lauric acid in a vertical rectangular cavity were investigated using both numerical simulations and experimental validation, as reported by [44,45]. In the experimental configuration, the cavity measured 5 cm wide and 12 cm high. The right vertical wall was maintained at a constant temperature of 70 °C, while the remaining walls were considered adiabatic. A comparison of the melt volume fraction of lauric acid of the present results with the results published by [45] is shown in Fig. 7. The close match between the present results and the published data in cited work, indicates that the model reliably captures phase change behavior within the defined thermal conditions.

In addition, Fig. 8 compares experimental observations of the melting front from [44] with simulation results obtained in this study. These comparisons show a high level of agreement, supporting the accuracy of the simulation when compared to experimental results.

4. Results and discussion

The parameters investigated in this study include the number of the petal ($0 \le n_p \le 8$), the amplitude of petal ($0.1 \le a_p \le 0.25$), petal radial offset ($1/4 \le e_p \le 5/4$), and petal prune. Table 3 summarizes the specifications of all 23 cases and shows the melting time (to reach MVF = 0.9) for each case separately. Fig. 9 illustrates how changing the number of petals from 3 to 8 affects the melting volume fraction over time. As shown, the melting process becomes faster with more petals. The time to reach 90% melting drops from 4081 s in Case C1 to 3286 s in Case C6, which is a 19.5% reduction. This improvement stems from a greater heat transfer surface and better flow circulation around the tube. However, after about six petals, the rate of improvement begins to slow down, due to thermal resistance near the outer PCM.

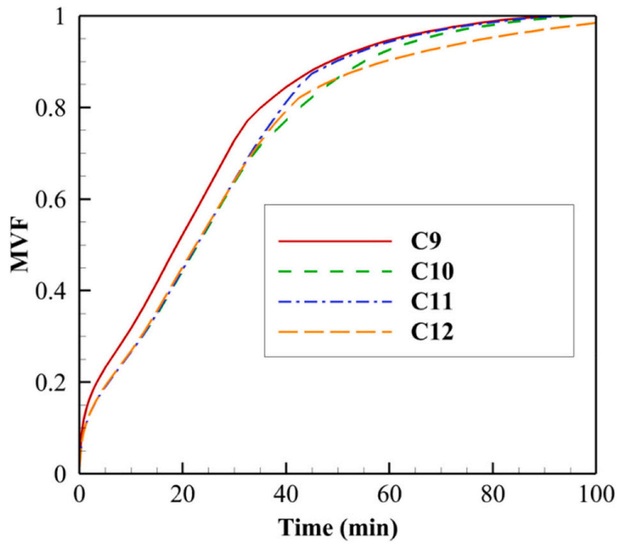

Fig. 13. Impact of petal removal (C9-C12 cases) on MVF during the charging process.

Increasing $n_p$enhances the HTF–PCM interfacial area and tip curvature, thinning the local thermal boundary layer and generating multiple buoyancy-driven plumes. This raises the early-stage global melting rate, observed as a steeper initial MVF slope $d(\text{MVF})/dt|_{t\leq 600\,\text{s}}$. Beyond 6 petals the inter-petal channels narrow, which damps lateral circulation and creates low-velocity pockets; the gain in area is then partially offset by convection suppression, explaining the diminishing returns after $n_p \geq 7$. Relative to $n_p = 3$, the initial MVF slope increases with $n_p = 6$, though the improvement is less pronounced for $n_p = 8$. Additionally, the time to reach 90% MVF (t_{90}) decreases from 4081 s to 3286 s, showing a notable reduction.

Fig. 10a illustrates the melting front at different times for Cases C1, C6, and C18. Case C6, with eight petals, shows a faster and wider spread of the melted region compared to the others. By 2400 s, a large portion of the PCM in C6 is already melted, especially around the petal tips, while in C1 and C18 much of the solid phase remains near the bottom. At 3600 s, C6 is nearly fully melted, whereas C1 and C18 still show clear unmelted zones. The broader, earlier red regions around petal tips arise from curvature-induced heat-flux intensification and plume merging above the upper tips; residual solid at the bottom reflects weaker buoyancy and longer conductive paths there. These results agree with Fig. 9, where C6 reaches 90% melting in 3286 s, about 19.5% faster than C1 and 43.6% faster than C18.

Fig. 10b illustrates the temperature distribution in phase changing process for three different cases C1, C6, and C18. In Case C6, the heat spreads more effectively from the petal tips, forming deeper and more irregular temperature zones. By 2400 s, the top region in C6 is almost fully heated, while C1 stays cooler near the shell and C18 shows horizontal layers with slower heat penetration. These observations support the trends in Fig. 9, where C6 reaches 90% melting much earlier than the others, confirming that more petals improve heat distribution and speed up melting.

Increasing the petal amplitude has a clear impact on the melting behavior. As shown in Fig. 11, the case with the smallest amplitude (C7, $a_\text{p} = 0.1$) reaches 90% melting after 4412 s, while the case with the highest amplitude (C9, $a_\text{p} = 0.25$) reaches it in just 2904 s. That's a reduction of about 34.2%. The curves show that as amplitude increases, the melting rate improves significantly due to better contact with the PCM and more active flow around the petal edges. However, the improvement becomes more gradual after ap = 0.2. At very high a_p, narrowed channels increase viscous losses and confine recirculation, so gains plateau; this is visible in the slower widening of isotherms away from tips at 2400–3600 s. drops from 4412 s ($a_p = 0.10$) to 2904 s ($a_p = 0.25$; −34.2%), while the MVF slope at 20–40 min rises.

Fig. 12a compares the melt fraction contours for Cases C7 and C9 at four time points. In the early stage (300 s), both cases show small melted regions, but C9 already exhibits deeper melt penetration near the petal tips. At 1200 s and 2400 s, the difference becomes more noticeable: C9 has a much wider melted area extending toward the shell, while C7 still retains large unmelted zones, especially near the bottom and corners. At 3600 s, Case C9 is nearly fully melted, whereas Case C7 still contains visible solid regions at the base. Based on the simulation data, C9 reaches 90% MVF in 2904 s, while C7 requires 4412 s to achieve the same level. This corresponds to a 34.2% reduction in melting time due to the higher petal amplitude ($a_\text{p} = 0.25$ in C9 vs. $a_\text{p} = 0.10$ in C7). The faster progression of the melting front in C9 seen in the contours confirms the trend observed in Fig. 11, where the MVF curve of C9 rises more steeply than that of C7.

Fig. 12b shows how temperature is distributed during melting for Cases C7 and C9. In the early stage (300 s), Case C9 shows stronger heat penetration around the petal tips, while in C7 the heat remains closer to the heat source. By 1200 s, the temperature in C9 extends more broadly and begins to heat the upper PCM layers, whereas in C7 the temperature field is still narrow with more noticeable layering. At 2400 s, a larger area in C9 reaches high temperatures, especially at the top, indicating more active natural convection. In contrast, C7 still shows a strong thermal gradient between the top and bottom. By 3600 s, Case C9 is almost uniformly heated, but C7 still has cooler zones near the base. This difference in temperature spread helps explain the faster melting in C9, which reaches 90% MVF in 2904 s compared to 4412 s in C7, a 34.2% improvement attributed to the greater petal amplitude. The faster thermal response in C9 observed here aligns with the earlier rise in its MVF curve in Fig. 11.

Cases C10–C12 shown in Fig. 13 explore modifications to the petal structure based on C9, which exhibited the best melting performance among symmetric configurations. These cases involve partial pruning and reshaping of the petals. All three curves follow a similar trend up to around 40 min, after which clear differences begin to emerge. The melting time increases moderately in C10 (3303 s) and more significantly in C12 (3541 s), corresponding to approximately 13.7% and 21.9% slower melting than C9 (2904 s), respectively. This suggests that excessive geometric modifications can interfere with the efficient heat transfer established in the original configuration. In contrast, C11, with moderate pruning, achieves 90% melting in 2980 s, about 2.6% faster than C9, indicating that minor surface trimming may enhance internal circulation and improve thermal distribution. The divergence observed in the MVF curves around 40 min is also reflected in the melt fraction contours (Fig. 14a), where the differences in melting progression become more apparent, particularly in the lower regions of the domain.

Fig. 14(a) depicts the impact of petal pruning on melting behavior by comparing three geometries: a fully featured petal structure (C10), a moderately pruned case (C11), and a heavily pruned one (C12). Although the number and size of petals remain the same, the trimming levels change the shape, affecting how heat spreads and how the PCM melts. At 300 s and 1200 s, C10 and C11 show evenly distributed melting around the petals with visible circulation zones, while C12 starts off less uniform due to its wide, flat tips. At 2400 s, C10 maintains balanced flow paths, but C12 shows disrupted and disconnected melting fronts. By 3600 s, C11 supports more complete melting, while C12 still retains solid PCM near the bottom. These patterns match the MVF trends in Fig. 13: all cases follow a similar path until around 40 min, after which C11 reaches 90% melting in 2980 s, slightly faster than C10 (3303 s), and significantly faster than C12 (3541 s), which is 21.9% slower than the optimal configuration C9 (2904 s).

Fig. 14(b) shows how temperature patterns reflect the melting differences. In the early stages (300–1200 s), all three cases begin heating near the petal edges, but C10 displays the most balanced distribution. C11 performs similarly, although its trimmed sides slightly reduce

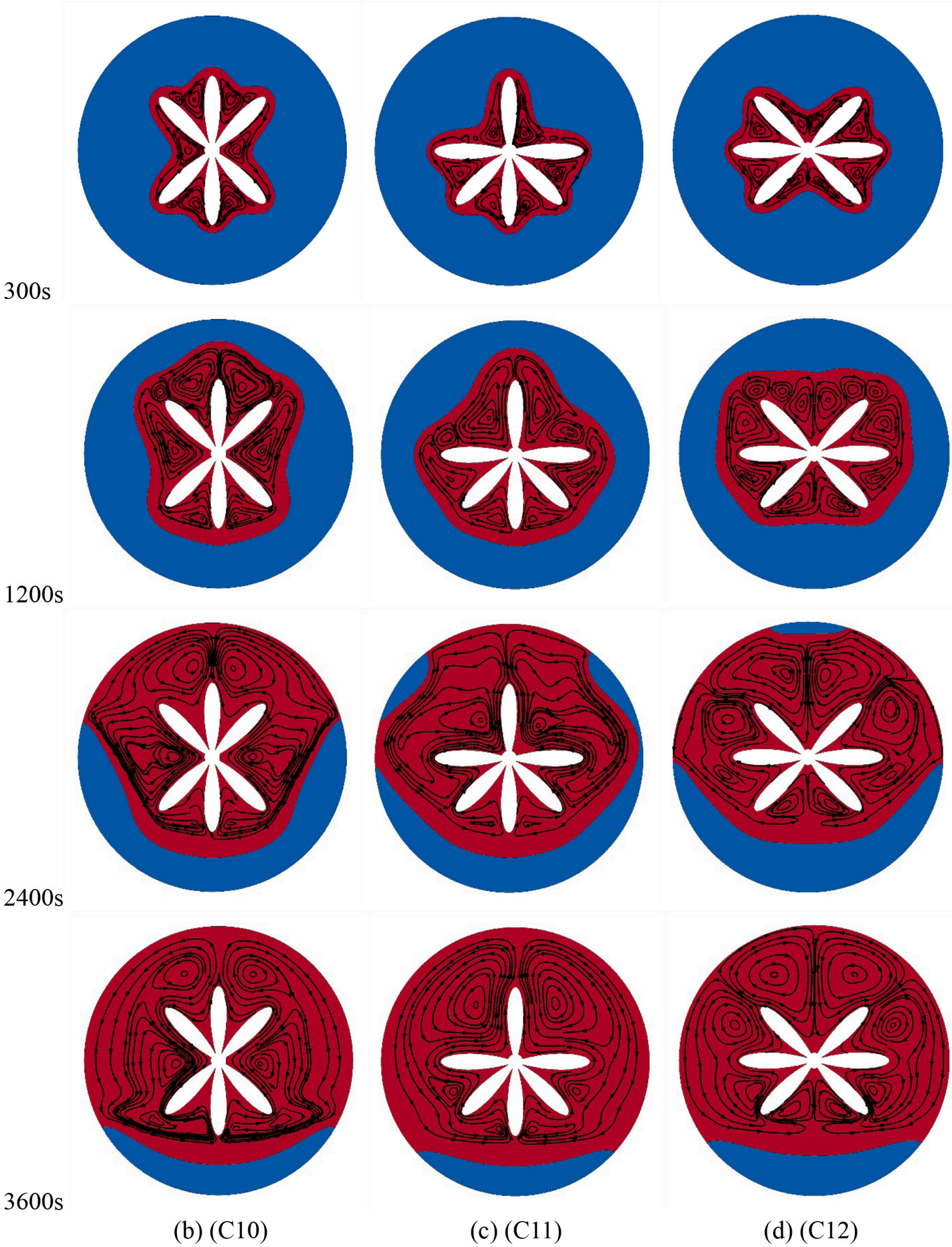

Fig. 14. (a) Impact of Petal prune on melting for (b) C10 (c) C11 (d) C12 at times: 300 s, 1200s, 2400 s, 3600 s. (b) Impact of Petal prune on thermal distribution for (b) C10 (c) C11 (d) C12 at times: 300 s, 1200s, 2400 s, 3600 s.

lateral heat spread. C12, in contrast, forms stronger vertical temperature layering and less effective heating of outer regions. At 2400 s and 3600 s, C10 develops a wide, connected hot region reaching deeper into the PCM, while C11 maintains good coverage. C12 continues to show uneven heating, particularly near the bottom. These trends confirm the MVF results in Fig. 13: C11's temperature field supports its near-optimal melting time of 2980 s, while C12's weaker thermal performance aligns with its delayed phase change at 3541 s. Moderate pruning (C11)

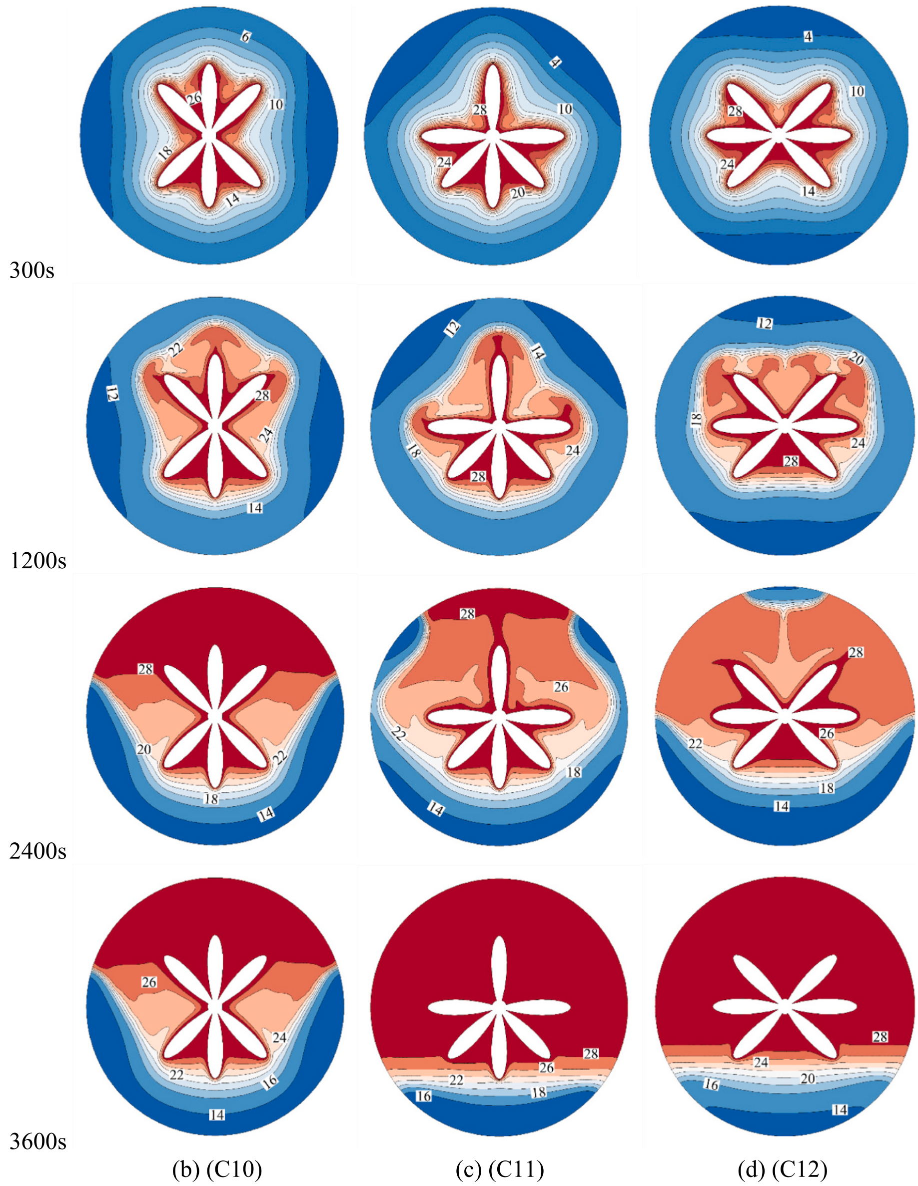

Fig. 14. (*continued*).

smooths sharp tip curvatures, reducing recirculation losses while maintaining sufficient area, hence a slight improvement over the fully featured C10 at mid-times; heavy pruning (C12) reduces both area and plume seeds, weakening natural convection and delaying front advancement. The more continuous melt front in C11 at 2400–3600 s indicates reduced lateral thermal resistance, whereas C12 shows disconnected fronts consistent with inhibited cross-lobe transport.

Fig. 15 illustrates how the petal radial offset (e_p) affects the melting process. Case C9, with a centered tube, is used as the geometric baseline. Up to around 20 min, all cases follow a similar trend in MVF, indicating that early-stage melting is not strongly influenced by radial offset. However, after this point, differences gradually appear. Among the eccentric configurations, Case C14 ($e_p = 1/2$) achieves the shortest melting time of 2675 s, making it about 7.9% faster than C9 and 38.6% faster than the circular reference case C20 (4343 s). Case C13 ($e_p = 1/4$) also performs very well, reaching 90% melting in 2695 s (7.2% faster than C9), while C15 ($e_p = 3/4$) records 2856 s (1.7% faster than C9). These results show that mild offsets improve heat distribution by enhancing asymmetric flow and natural convection. On the other hand, larger eccentricities reduce performance: C16 ($e_p = 1$) takes 3119 s (7.4% slower than C9), and C17 ($e_p = 5/4$) needs 3421 s, which is 17.8% slower. This trend suggests that a moderate shift away from the center can enhance melting efficiency, but excessive displacement leads to uneven heat distribution and slower phase change. Small–moderate e_p breaks symmetry and creates a dominant recirculation cell on the near side, shortening the conductive path to the hot wall and boosting MVF early. Large offsets shift the structure too close to one side, producing far-side stagnant zones and reduced plume interaction; MVF then lags despite local near-wall intensification. Optimal cases (e.g., C14, $e_p = 1/2$) achieve $t_{90} = 2675$s (−7.9% vs C9), whereas excessive offsets (C17, 5/4) extend t_{90} to 3421 s (+17.8%).

Fig. 16 compares the melting performance of non-petal cases (C18–C23) with different levels of eccentricity. Up to around 50 min, all curves follow nearly the same path, indicating that eccentricity has little effect on the early stages of melting. This observation aligns with the melt fraction contours in Fig. 17a, which show similar patterns during initial times. After this point, however, the impact of radial offset becomes clearer. Case C21 ($e_p = 3/4$) shows the best performance, reaching 90% melting in 4247 s, which is approximately 27% faster than the centered reference C18 (5822 s). Other improved cases include C20

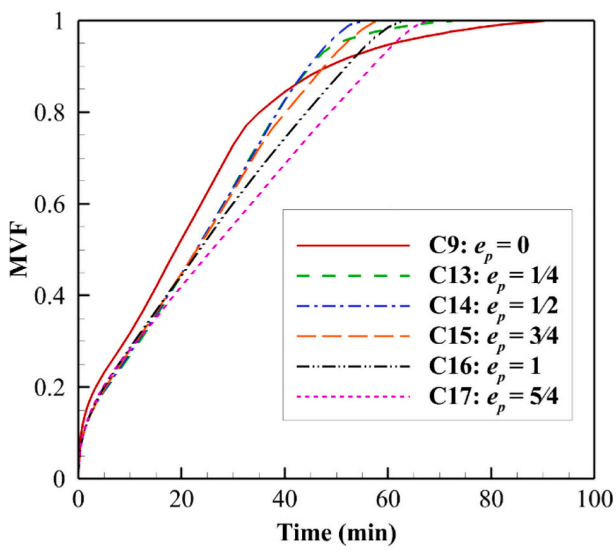

Fig. 15. Impact of radial offset on the MVF during the charging process for petal cases.

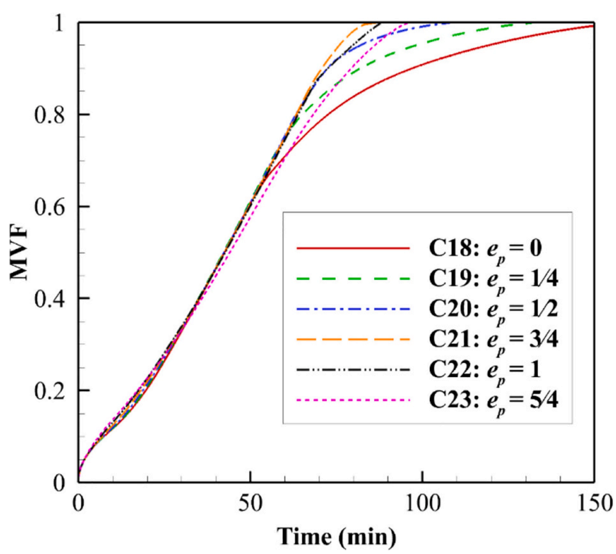

Fig. 16. Impact of radial offset on the MVF during the charging process for cylindrical cases (non-petal).

($e_p = 1/2$) at 4343 s (25.4% faster than C18) and C19 ($e_p = 1/4$) at 4916 s (15.5% faster than C18). In contrast, larger offsets begin to degrade performance: C22 and C23 require 4352 s and 4760 s, respectively. These results suggest that mild eccentricity can improve heat spread even without petal structures, but excessive offsets reduce efficiency by causing thermal asymmetry and weaker convection in the far regions. Contours at 1200–2400 s show hotter, thicker upper layers on the near side for C21, while the far side remains stratified, direct evidence of asymmetric convection controlling the trend.

In all cylindrical cases (C18–C23), the radial offset is applied downward (in the direction of gravity), positioning the HTF tube closer to the lower shell wall. The upper region of the system experiences stronger natural convection and therefore melts more quickly than the lower region. By contrast, the lower region is weakly circulated and tends to melt more slowly. For this reason, applying eccentricity downward is the most effective strategy: it enhances heat transfer specifically in the thermally weaker lower region, where improvement is most needed.

Fig. 17a illustrates how shifting the petal structure away from the center affects the melting front. At 1200 s, the melt front in all three cases, C13, C17, and C21, appears similar, which agrees with Fig. 16 showing nearly identical MVF trends during the first 50 min. As melting progresses, differences become clearer. In C13, the slight offset creates asymmetry that enhances circulation on one side, helping heat spread more evenly and supporting relatively fast melting. C14 and C15 show even stronger performance, benefiting from a more pronounced lateral shift while still preserving balanced flow, C14 reaches 90% MVF in 2675 s and C15 in 2856 s, which is 7.9% and 1.7% faster than C9, respectively. These results highlight that moderate eccentricity can significantly enhance the melting front by directing thermal energy more effectively. In contrast, larger offsets like in C17 and C21 cause the heat to concentrate near one wall, leaving the opposite side cooler and slowing the melt in those regions. By 3600 s, C21 still shows the most advanced melting front, with minimal solid PCM remaining, confirming the trend seen in Fig. 16, where C21 reached 90% melting in 4247 s, around 27% faster than the fully centered case C18 (5822 s). These contours clearly demonstrate that moderate eccentricity helps the melting process, while excessive shifting reduces efficiency.

Fig. 17b shows how the radial position of the tube affects temperature distribution within the PCM. In C13, the temperature field is well balanced, with heat spreading symmetrically around the lobes. This uniformity supports efficient heat flow and helps accelerate melting. As the offset increases, this balance begins to break down. In C14 ($e_p = 1/2$), although the temperature field becomes slightly asymmetric, the overall spread remains effective across the domain, contributing to the best melting performance among all configurations, reaching 90% MVF in just 2675 s, which is 7.9% faster than the previously optimal case C9 (2904 s) and 38.4% faster than the circular base case C20. C15 also maintains good thermal reach despite some distortion, achieving 90% melting in 2856 s (1.7% faster than C9). In contrast, C17 and especially C21 suffer from clear asymmetries: in C17, heat clusters near petal tips with weak lateral conduction, while in C21, one side becomes overheated while the other remains underheated. Despite this, C21 still completes melting in 4247 s (27% faster than C18), due to localized convective loops. These patterns confirm that slight to moderate offset improves heat circulation, but excessive displacement compromises thermal balance and limits overall melting efficiency.

5. Conclusion

This study explored the role of internal geometry in shaping the thermal efficiency of a LHTES unit using a petal-shaped heat exchanger. A total of 23 configurations were analyzed by studying four key design parameters: petal number (n_p), petal amplitude (a_p), degree of pruning, and radial offset (e_p). The impact of each parameter was measured by tracking melting duration, temperature patterns, and flow behavior inside the PCM.

This work establishes a geometry-based parametric framework for shell-and-tube LHTES, isolating convection effects by varying petal number and amplitude at constant HTF area, quantifying the capacity–power trade-off through petal-removal cases (increased PCM mass vs. reduced interfacial area), and revealing buoyancy coupling via gravity-aligned eccentricity, an integrated perspective not jointly addressed in prior studies.

Considering number of petals, adding more petals enlarged the thermal exchange surface and helped the melted material circulate better, resulting in faster and more complete melting. The configuration with eight petals (C6) achieved significantly better performance than cases with fewer or no petals. Specifically, it led to a 19.5% decrease in melting duration relative to the three-petal case (C1) and a 43.6% decrease compared to the circular non-petal case (C18).

In terms of petal amplitude, larger amplitudes (e.g., $a_p = 0.25$) accelerated melting and improved thermal penetration. Compared to the smallest amplitude ($a_p = 0.10$, Case C7), the highest amplitude (C9)

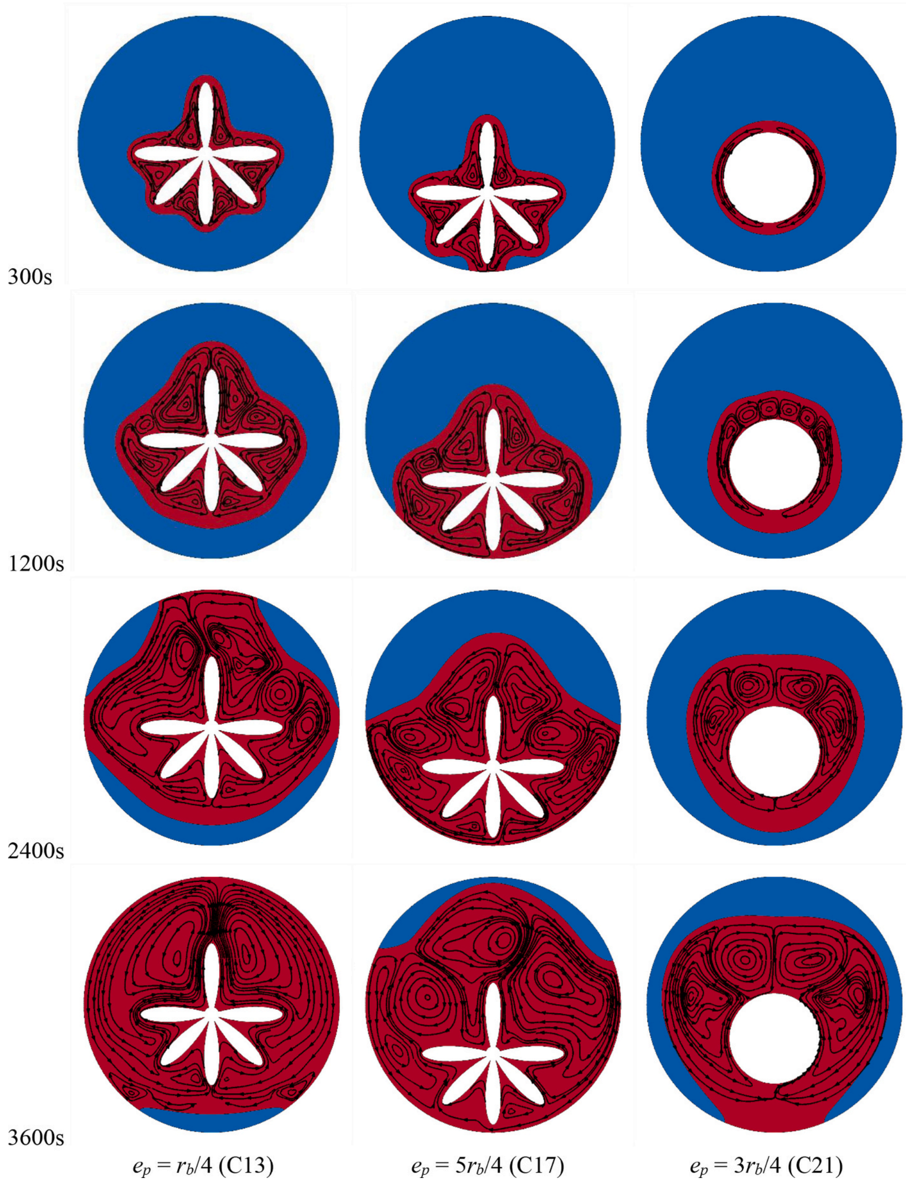

Fig. 17. (a) Impact of radial offset on melting process for $e_p = 1/4$ (C13), $e_p = 5/4$ (C17), $e_p = 3/4$ (C21) at times: 300 s, 1200s, 2400 s, 3600 s. (b) Impact of the radial offset for on thermal distribution for $e_p = 1/4$ (C13), $e_p = 5/4$ (C17), $e_p = 3/4$ (C21) at times: 300 s, 1200s, 2400 s, 3600 s.

reduced the melting time by approximately 34.2%.

To study the effect of pruning, while removing a small amount of the petal surface had little negative effect, excessive removal reduced thermal contact and disrupted flow paths. The most heavily pruned case (C12) showed a 21.9% slower melting time than C9, while the moderately pruned case (C11) even slightly outperformed C9 by 2.6%.

For the radial position effect, slightly off-center arrangements (e.g., C21 with $e_p = 3/4$) helped improve flow symmetry and heat transport. Compared to the centered circular configuration (C18), C21 reduced the melting duration by 27%. However, extreme offsets (e.g., C23) caused thermal imbalance and left large solid zones at the bottom, slowing melting efficiency.

All in all, the most efficient case among symmetric geometries was C9, with eight petals, high amplitude, no pruning, and a centered layout. It demonstrated a melting time of 2904 s, which represents a 33.1% reduction compared to the reference case (C20, 4343 s), highlighting how strategic geometric design can greatly enhance LHTES performance. Interestingly, cases C13, C14, and C15 with moderate radial offsets, achieved even shorter melting durations, with C14 reaching 2675 s, corresponding to a 38.4% improvement.

CRediT authorship contribution statement

Mohamed Bouzidi: Writing – review & editing, Writing – original draft, Validation, Investigation, Formal analysis, Data curation, Conceptualization. **Mohammad Hossein Heidarshenas:** Writing – original draft, Visualization, Methodology, Investigation, Formal analysis, Data curation. **Mohammed Hasan Ali:** Writing – review & editing, Writing – original draft, Visualization, Software, Investigation, Formal analysis, Data curation, Conceptualization. **T. Anwor:** Writing – review & editing, Writing – original draft, Resources, Methodology, Investigation, Funding acquisition, Conceptualization. **Mansour Mohamed:** Writing – review & editing, Visualization, Methodology, Funding acquisition, Formal analysis, Data curation. **Hammadi Khmissi:** Writing – review & editing, Writing – original draft, Validation, Resources, Investigation, Funding acquisition, Data curation,

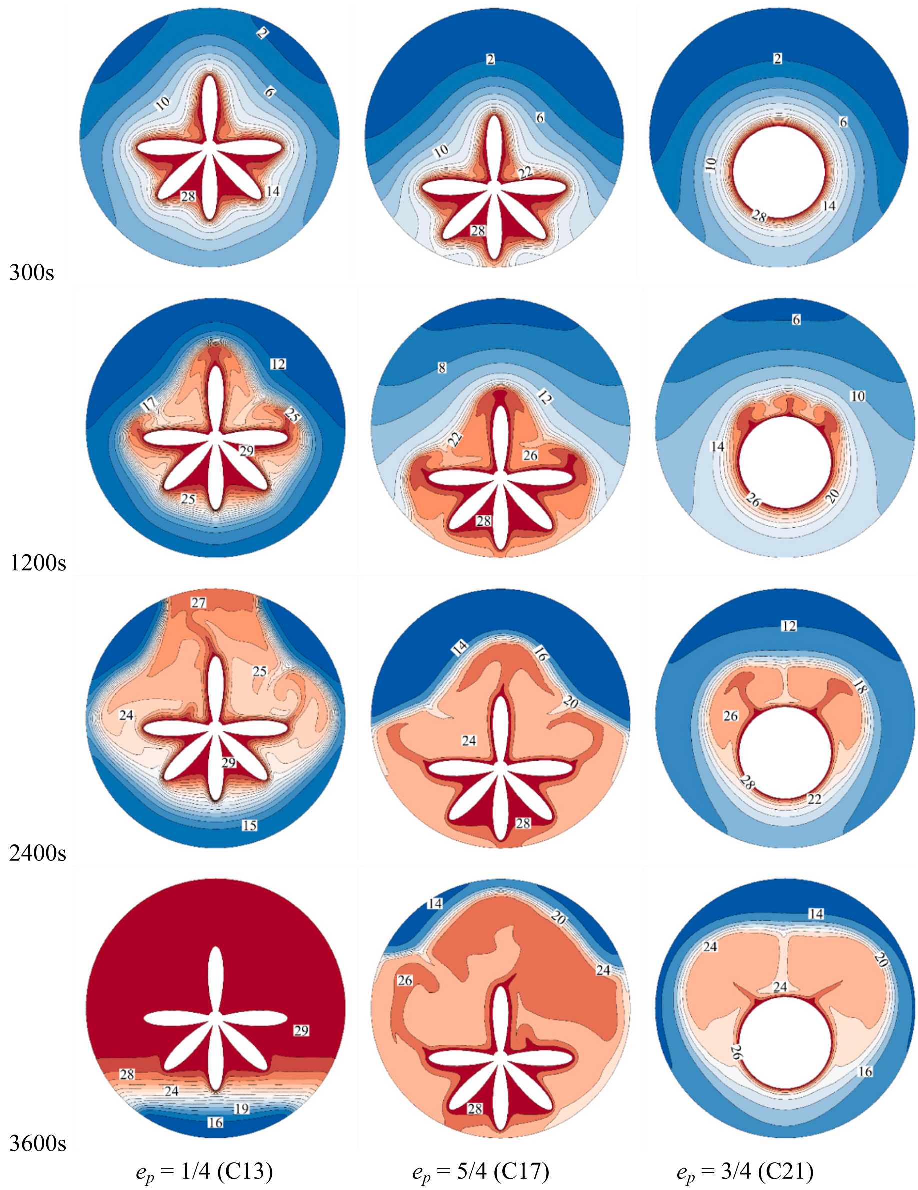

Fig. 17. (*continued*).

Conceptualization. **Zehba Raizah:** Writing – review & editing, Writing – original draft, Visualization, Validation, Software, Methodology. **Bhupendra Singh Chauhan:** Writing – review & editing, Visualization, Methodology, Investigation, Data curation, Conceptualization. **Mehdi Ghalamba:** Writing – review & editing, Writing – original draft, Visualization, Validation, Supervision, Project administration.

Declaration of competing interest

The authors declare that they have no known competing financial interests or personal relationships that could have appeared to influence the work reported in this paper.

Acknowledgement

The authors extend their appreciation to the Deanship of Scientific Research at King Khalid University, Abha, Saudi Arabia, for funding this work through the Research Group Project under Grant Number (RGP2/395/46). The authors extend their appreciation to the Deanship of Scientific Research at Northern Border University, Arar, KSA for funding this research work through the project number "NBU-FPEJ-2026-2222-02".

Data availability

Data will be made available on request.

References

[1] H. Togun, H.S. Sultan, H.I. Mohammed, A.M. Sadeq, N. Biswas, H.A. Hasan, R. Z. Homod, A.H. Abdulkadhim, Z.M. Yaseen, P. Talebizadehsardari, A critical review on phase change materials (PCM) based heat exchanger: different hybrid techniques for the enhancement, J. Energy Storage 79 (2024) 109840.

[2] K. Liu, C. Wu, H. Gan, C. Liu, J. Zhao, Latent heat thermal energy storage: theory and practice in performance enhancement based on heat pipes, J. Energy Storage 97 (2024) 112844.

[3] A. Nandi, N. Biswas, A. Datta, N.K. Manna, D.K. Mandal, S. Biswas, A comprehensive review on enhanced phase change materials (PCMs) for high-performance thermal energy storage: progress, challenges, and future perspectives, J. Therm. Anal. Calorim. (2025) 1–44.

[4] S. Shen, H. Zhou, Y. Du, Y. Huo, Z. Rao, Investigation on latent heat energy storage using phase change material enhanced by gradient-porosity metal foam, Appl. Therm. Eng. 236 (2024) 121760.

[5] K. Zhang, H. Li, L. Wang, K. Song, Q. Zhang, G. Shi, Experimental investigation on the thermal performance of longitudinally finned tube latent heat thermal energy storage unit, Appl. Therm. Eng. 279 (2025) 127690.
[6] I. Benyahia, M.F. Al-Ghamdi, A. Abderrahmane, O. Younis, S. Laouedj, K. Guedri, A. Alahmer, Comprehensive thermal analysis of a nano-enhanced PCM in a finned latent heat storage system, Int. Commun. Heat Mass Transf. 165 (2025) 109106.
[7] M. Rahman, R. Zairov, N. Akylbekov, R. Zhapparbergenov, S. Hasnain, Pioneering heat transfer enhancements in latent thermal energy storage: passive and active strategies unveiled, Heliyon 10 (19) (2024) e37981.
[8] Z.H. Low, Z. Qin, F. Duan, A review of fin application for latent heat thermal energy storage enhancement, J. Energy Storage 85 (2024) 111157.
[9] W. Zhang, L. Pan, D. Ding, R. Zhang, J. Bai, Q. Du, Progress in the study of enhanced heat exchange in phase change heat storage devices, ACS Omega 8 (2023) 22331–22344.
[10] R. Hamid, Z. Mehrdoost, Thermal performance enhancement of multiple tubes latent heat thermal energy storage system using sinusoidal wavy fins and tubes geometry modification, Appl. Therm. Eng. 245 (2024) 122750.
[11] M. Saqib, R. Andrzejczyk, A review of phase change materials and heat enhancement methodologies, Wiley Interdiscip. Rev. Energy Environ. 12 (2023) e467.
[12] J. Pereira, A. Moita, A. Moreira, An overview of the nano-enhanced phase change materials for energy harvesting and conversion, Molecules 28 (2023) 5763.
[13] S. Tian, J. Ma, S. Shao, Q. Tian, Z. Wang, Y. Zhao, B. Tan, Z. Zhang, Z. Sun, Estimation of heat transfer performance of latent thermal energy storage devices with different heat transfer interface types: a review, J. Energy Storage 86 (2024) 111315.
[14] Lithium ion battery thermal management system and method based on phase change material and mutually-embedded fins Lithium-Ion Battery Thermal Management System and Method Based on Phase Change Materials and Interlocking Fins, in: China National Intellectual Property Administration, 2022.
[15] Battery thermal management system, control method thereof and vehicle air conditioning system Battery Thermal Management System, Its Control Method, and Vehicle Air Conditioning System, in: China National Intellectual Property Administration, 2023.
[16] S. Pandey, Y.G. Park, M.Y. Ha, An exhaustive review of studies on natural convection in enclosures with and without internal bodies of various shapes, Int. J. Heat Mass Transf. 138 (2019) 762–795.
[17] A. Abdulkadhim, I.M. Abed, N. Mahjoub Said, Review of natural convection within various shapes of enclosures, Arab. J. Sci. Eng. 46 (2021) 11543–11586.
[18] N.C. Roy, Natural convection of nanofluids in a square enclosure with different shapes of inner geometry, Phys. Fluids 30 (2018).
[19] Z. Raizah, A.M. Aly, Natural convection from heated shape in nanofluid-filled cavity using incompressible smoothed particle hydrodynamics, J. Thermophys. Heat Transf. 33 (2019) 917–931.
[20] F. Ilinca, J.-F. Hétu, Immersed boundary solution of natural convection in a square cavity with an enclosed rosette-shaped hot cylinder, Numer. Heat Transf. A Appl. 65 (2014) 1154–1175.
[21] J. Wołoszyn, K. Szopa, Shell shape influence on latent heat thermal energy storage performance during melting and solidification, Energies 16 (2023) 7822.
[22] Z.-C. Sun, W. Li, X. Ma, L.-X. Ma, H. Yan, Two-phase heat transfer in horizontal dimpled/protruded surface tubes with petal-shaped background patterns, Int. J. Heat Mass Transf. 140 (2019) 837–851.
[23] Z. Cheng, J. Du, S. Jia, C. Xiao, F. Jiao, Y. Hong, Impact of tube shapes on the energy storage and thermal-hydraulic performances of finned latent heat energy storage systems, Case Studies in Therm. Eng. 67 (2025) 105827.
[24] J. Shafi, O. Younis, S. Tiari, M. Ghalambaz, Artificial intelligence – numerical study of melting and solidification heat transfer in a bundle of petal tubes embedded in metal foam, Appl. Therm. Eng. 279 (2025) 127960.
[25] M.E. Zayed, J. Zhao, W. Li, A.H. Elsheikh, A.M. Elbanna, L. Jing, A. Geweda, Recent progress in phase change materials storage containers: geometries, design considerations and heat transfer improvement methods, J. Energy Storage 30 (2020) 101341.
[26] Q. Mao, K. Chen, T. Li, Heat transfer performance of a phase-change material in a rectangular shell-tube energy storage tank, Appl. Therm. Eng. 215 (2022) 118937.
[27] M. Kadivar, M. Moghimi, P. Sapin, C. Markides, Annulus eccentricity optimisation of a phase-change material (PCM) horizontal double-pipe thermal energy store, J. Energy Storage 26 (2019) 101030.
[28] M.A. Alnakeeb, M.M. Sorour, A.O. Alkadi, A.A. Gomaa, A.M. ELghoul, M. M. Zaytoun, The influence of elliptic aspect ratio and inclination angle on the melting characteristic of phase change material in concentric cylindrical enclosure, J. Energy Storage 62 (2023) 106832.
[29] M. Eisapour, A.H. Eisapour, A. Shafaghat, H.I. Mohammed, P. Talebizadehsardari, Z. Chen, Solidification of a nano-enhanced phase change material (NePCM) in a double elliptical latent heat storage unit with wavy inner tubes, Sol. Energy 241 (2022) 39–53.
[30] M. Dongellini, G. Martino, C. Naldi, S. Lorente, G.L. Morini, Experimental study on the heat transfer performance of finned-tube heat exchangers in latent thermal energy storages: effects of PCM types and operating conditions, Appl. Therm. Eng. 271 (2025) 126273.
[31] S. Mehryan, K. Raahemifar, S.R. Ramezani, A. Hajjar, O. Younis, P. Talebizadeh Sardari, M. Ghalambaz, Melting phase change heat transfer in a quasi-petal tube thermal energy storage unit, PLoS One 16 (2021) e0246972.
[32] S. Zhou, H. Dai, M. Gao, S. He, P. Niu, Y. Shi, J. Qi, F. Sun, Influence of inner tube shapes on the charging and discharging performance for the latent heat thermal storage exchangers, Int. Commun. Heat Mass Transf. 154 (2024) 107466.
[33] S. Chavan, R. Rudrapati, S. Manickam, A comprehensive review on current advances of thermal energy storage and its applications, Alex. Eng. J. 61 (2022) 5455–5463.
[34] J.P. Da Cunha, P. Eames, Thermal energy storage for low and medium temperature applications using phase change materials–a review, Appl. Energy 177 (2016) 227–238.
[35] A.I.N. Korti, H. Guellil, Experimental study of the effect of inclination angle on the paraffin melting process in a square cavity, J. Energy Storage 32 (2020) 101726.
[36] A. Agarwal, R. Sarviya, Characterization of commercial grade paraffin wax as latent heat storage material for solar dryers, Mater. Today Proc. 4 (2017) 779–789.
[37] N. Ukrainczyk, S. Kurajica, J. Šipušić, Thermophysical comparison of five commercial paraffin waxes as latent heat storage materials, Chem. Biochem. Eng. Q. 24 (2010) 129–137.
[38] N.B. Khedher, M. Sheremet, A.M. Hussin, S.A.M. Mehryan, M. Ghalambaz, The effect of hot wall configuration on melting flow of nano-enhanced phase change material inside a tilted square capsule, J. Energy Storage 69 (2023) 107921.
[39] H. Zheng, C. Wang, Q. Liu, Z. Tian, X. Fan, Thermal performance of copper foam/paraffin composite phase change material, Energy Convers. Manag. 157 (2018) 372–381.
[40] R. Karami, B. Kamkari, Investigation of the effect of inclination angle on the melting enhancement of phase change material in finned latent heat thermal storage units, Appl. Therm. Eng. 146 (2019) 45–60.
[41] J. Xie, K.F. Choo, J. Xiang, H.M. Lee, Characterization of natural convection in a PCM-based heat sink with novel conductive structures, Int. Commun. Heat Mass Transf. 108 (2019) 104306.
[42] N.B. Khedher, M. Ghalambaz, A.S. Alghawli, A. Hajjar, M. Sheremet, S.A. M. Mehryan, Study of tree-shaped optimized fins in a heat sink filled by solid-solid nanocomposite phase change material, Int. Commun. Heat Mass Transf. 136 (2022) 106195.
[43] J.N. Reddy, D.K. Gartling, The Finite Element Method in Heat Transfer and Fluid Dynamics, CRC Press, 2010.
[44] B. Kamkari, H. Shokouhmand, F. Bruno, Experimental investigation of the effect of inclination angle on convection-driven melting of phase change material in a rectangular enclosure, Int. J. Heat Mass Transf. 72 (2014) 186–200.
[45] B. Kamkari, H.J. Amlashi, Numerical simulation and experimental verification of constrained melting of phase change material in inclined rectangular enclosures, Int. Commun. Heat Mass Transf. 88 (2017) 211–219.